Detection of UXO in Underwater Sites Using Towed Array Resistivity/IP Measurements

SERDP Project UX-1325

FINAL TECHNICAL REPORT

Submitted March 10, 2004

Donald D. Snyder, and Scott C. MacInnes
Zonge Engineering & Research Organization, Inc
3322 E. Fort Lowell Road
Tucson, AZ 85716
skips@bresnan.net
zonge@alaska.net

Douglas LaBrecque, and Roger Sharpe
MPT, LLC
Reno, NV

Table of Contents

1. Introduction

1.1 Background

This research has been conducted in response to the statement of need UXSON-02-04 calling for research into new techniques for locating UXO in underwater environments. Electrical methods, particularly the induced polarization response (IP), respond to metal objects. But on land, electrical methods have low productivity and require the intrusive placement of electrodes into the ground. If for no other reason, this requirement for making "galvanic" electrical contact with the earth would seem to preclude the use of these methods over land. Water, however, is a medium that provides good galvanic contact and therefore permits electrical methods including the dynamic measurement of resistivity and IP. Hence, in principle, there are neither safety nor productivity issues with deploying these methods should they prove useful.

Induced Polarization (IP) is an electrical phenomenon associated with capacitive-like effects at interfaces between electrolytic pore fluids and solids. Media containing small amounts of metallic minerals (e.g., metallic sulfides) or clay minerals will have an associated IP response. The presence of IP associated with disseminated mineralization provides the basis for a very successful method of mineral exploration. It is well known, however, that IP responses are also associated with buried metallic culture (e.g., fences, well casing, pipes, and culverts). In mineral exploration, this "cultural noise" is to be avoided. In the context of the detection of UXO, however, this "cultural noise" is the desired target. Thus, in principle, galvanic electrical measurements, IP in particular, can be used for the detection of UXO.

It is not well known, even among geophysicists, that an early application of IP was military. During World War II, the Navy Ordnance Laboratory (NOL) developed the RX-1 Beach Mine Locator which was based on the principle of "Induced Electrical Potential" or IEP [4]. After the war, two of the participants in the NOL's mine locator project were involved in further research and development of IEP for mineral exploration. David Bleil completed a landmark thesis on the IP method in 1948 [5]. Ed McAlister left the navy after the war and joined the Anaconda Company where he was chief geophysicist. Newmont Mining began research and development on the IP method in 1946 and rightfully deserves much of the credit for early development of the IP method. According to Art Brant, who headed the effort, the Newmont research started upon advice from the Radio Frequency Lab in Boontown, NJ of a polarization phenomenon arising when metallic objects submerged in a water tank were subjected to periodic pulses of current [6]. In his review of the history of the IP method, Grow [4] suggests that "The origin of this information was almost certainly the mine locator project of the NOL".

All of the information about the RX-1 Beach Mine Locator is anecdotal. Apparently, all technical reports and descriptions of the apparatus and its design have been destroyed. The purpose of this research, therefore, has been to re-establish IP as a viable method for detection of metallic objects (UXO, for example) in a fluid saturated medium. Our effort was funded by SERDP for a period of 1 year. Our objective has been, at minimum expense, to test the feasibility of using towed-array IP measurements as a basis for detecting UXO in shallow water.

Over the last year we have conducted laboratory-scale model experiments and numerical model experiments in an effort to establish the scale of the response. Based on our model results, we designed a simple electrode array. We made minor modifications to the existing IP software in

Zonge's GDP-32^{II} multifunction receiver, and we tested the resulting system at the Mare Island Naval Shipyard in San Francisco Bay. We describe each phase of our investigation in detail in the remainder of this report.

2. Induced Polarization Phenomenology

2.1 Electrode Overvoltage

In the context of UXO detection, the term Induced Polarization refers to an impedance that exists across the boundary between an electronic conductor (e.g. a metal) and an electrolyte.[1] The reactions that occur at the boundary between an electrode and the electrolyte are complex and we will not attempt to explain them in detail. A concise explanation of the electrochemistry that occurs at the electrode boundary may be found in Sumner (chapter 3) [3]. When the electrode is in equilibrium with the electrolyte, a small equilibrium potential is set up across the boundary. The equilibrium potential is the sum of chemical and electrostatic forces resulting from the slight solubility of the metal in contact with the solution. When small currents (i.e. < 1μA/cm^2) are driven across the boundary, the potential difference across the boundary changes. The difference between the potential difference in the driven condition and the equilibrium potential is called the Overvoltage potential. Overvoltage represents the energy required to drive the electrochemical reactions required to affect the transfer of electrons and thus the mode of conduction from electrolytic to electronic. At low current densities, the overvoltage is proportional to current density and the constant of proportionality, known as the polarization resistance, depends on the electrode composition, the electrolyte chemistry, the temperature, and the direction of the current (i.e., into or out of the boundary).

Overvoltage is a function of frequency that means that when stimulating the electrode with time varying current densities, the polarization resistance is actually a polarization impedance. At frequencies typically used in exploration (i.e., f < 100 Hz), surface impedance at the boundary between the metal and the solution is dominated by the diffusion of ions to the metal surface at which point the ion is oxidized or reduced by giving up or accepting electrons supplied by the metal. The behavior of that impedance as a function of frequency cannot be characterized as a simple capacitor. Graeme [7] noted that the impedance varied inversely with the square root of the frequency (f) and introduced a theoretical lumped circuit element, the "Warburg Impedance" to model the impedance at the boundary. The Warburg impedance behaves according to the relation

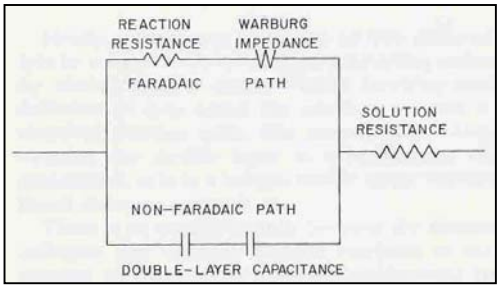

Figure 2.01: Equivalent circuit representing impedance across an electrode boundary. (After Sumner [4])

$$W = \frac{K}{(j\omega)^{\frac{1}{2}}}; \text{ where } K \text{ is a real constant, } j = \sqrt{-1} \qquad (1)$$

[1] We describe here the phenomenon of *electrode polarization* because it is the mechanism by which metallic conductors can be detected with observations of IP. A second mechanism, *membrane polarization*, is related to the presence of platy silicate minerals (e.g., clays) in an otherwise non-reactive porous medium.

Figure 2.01 is a circuit model taken from Sumner [3] that illustrates the two major paths for current conduction across an electrode boundary. The W element in the Figure indicates the Warburg impedance. At low frequencies, the circuit branch containing the Warburg element (labeled "Faradaic Path") has the higher conductance (lower impedance) and therefore carries most of the current. The conductance of circuit branch labeled "Non-Faradaic Path" becomes important at higher frequencies. At these frequencies, current is passed across the boundary through a capacitive mechanism similar to a dielectric. In Figure 2.02, we show an idealized spectrum of the impedance across an electrode boundary as a function of frequency. The log-log linear region labeled the "Warburg Region" covers the frequency range where, in practice, we measure IP.

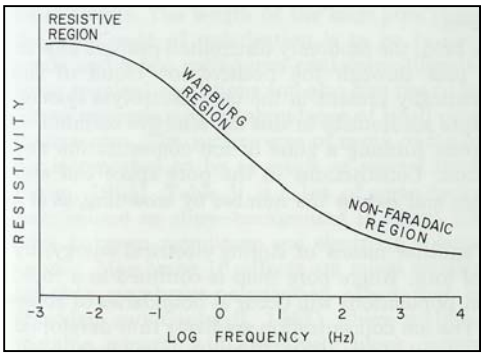

Figure 2.02: Idealized spectrum depicting the frequency behavior of the impedance across an electrode boundary. (Sumner, [4])

It is worthwhile to examine the behavior of a spherically-shaped conductive body in a uniform current field. The derivation substantially follows the classic problem in electrostatic fields (see for example Stratton, p. 205 [8]). In this case, however, we add a thin layer outside the sphere that has a complex transverse resistance λ [9].[2] The following derivation is similar to one presented in Wait [10] (Chapter II). The geometry is shown in Figure 2.03.

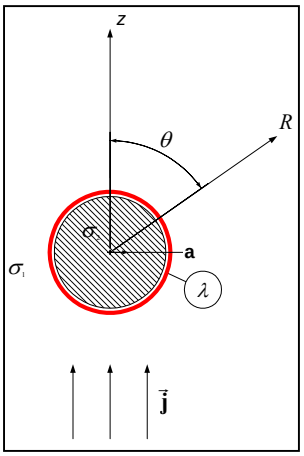

Figure 2.03: Sphere geometry.

In terms of a potential field, we write the primary potential as

$$\phi_o = \frac{J}{\sigma_1} R\cos\theta \qquad (2a)$$

We write the total potential external to the sphere as the sum of the primary potential (2a) plus a series of spherical harmonics

$$\phi_e = \phi_0 + \delta\phi = \frac{J}{\sigma_1} R\cos\theta + \sum_{i=0}^{\infty} \frac{B_i}{R^{i+1}} P_i(\cos\theta) \qquad (2b)$$

where P_i is the n^{th} degree Legendre polynomial.

Similarly, we write the potential internal to the sphere as a series of spherical harmonics

[2] Taking a cue from Keller and Frischknecht, we define the complex transverse resistance (better *transverse impedance*) as the product of a theoretical complex resistivity multiplied by a unit of length. Bound up in this parameter is the amplitude and frequency behavior of electrode overvoltage.

$$\phi_i = \sum_{n=0}^{\infty} A_n R^n P_n(\cos\theta) \qquad (3)$$

The unknown coefficients are found by enforcing boundary conditions at the coordinate R=a (i.e., the boundary of the sphere). In the classic problem, these conditions demand that we force the potential and the normal component of the current density (j) to be continuous across the boundary. But in this case, we have added a thin layer of conductance λ so there must be a potential drop across this layer. The boundary conditions are therefore

$$\sigma_1 \frac{\partial \phi_e}{\partial R}\Big|_{R=a} = \sigma_2 \frac{\partial \phi_i}{\partial R}\Big|_{R=a}; \text{ continuity of current density} \qquad (4)$$

$$\phi_e - \phi_i = \lambda \sigma_1 \frac{\partial \phi_e}{\partial R}\Big|_{R=a} \qquad (5)$$

The second boundary condition (equation 5), demands that there be a discontinuity in potential across the boundary of the sphere that is proportional to the electric field, with the constant of proportionality equal to the surface conductance parameter λ.

When equations 2b, 3, 4, and 5 are solved, we find as in the classic problem that there is only single non-Zero coefficient in equation 2b,

$$B_1 = \frac{a\sigma_1 + (\lambda\sigma_e - a)\sigma_2}{2\sigma_1 a + (a + 2\lambda\sigma_1)\sigma_2}\left(\frac{a^3 J}{\sigma_1}\right) \qquad (6)$$

Note that when λ=0, equation 6 degenerates to the classic solution for the standard problem which is

$$B_1 = \frac{\sigma_1 - \sigma_2}{2\sigma_1 + \sigma_2}\left(\frac{a^3 J}{\sigma_1}\right) \qquad (6a)$$

The resulting external potential, the one that we would measure, is written by substituting equation 6 into equation 2b

$$\phi_e = \frac{J}{\sigma_1} R\cos\theta + B_1 \frac{\cos\theta}{R^2} = \frac{J}{\sigma_1} R\cos\theta + \frac{a\sigma_1 + (\lambda\sigma_1 - a)\sigma_2}{2\sigma_1 a + (a + 2\lambda\sigma_1)\sigma_2}\left(\frac{a^3 J}{\sigma_1}\right)\frac{\cos\theta}{R^2} \qquad (7)$$

The second term in equation 7 can be recognized as representing the potential of a point dipole located at the origin of coordinates (R=0). The moment of the dipole is

$$\begin{aligned} M &= 4\pi a^3 \frac{a\sigma_1 + (\lambda\sigma_1 - a)\sigma_2}{2\sigma_1 a + (a + 2\lambda\sigma_1)\sigma_2}\left(\frac{J}{\sigma_1}\right) = -\chi E_0 \\ \chi &= 4\pi a^3 \frac{a\sigma_1 + (\lambda\sigma_1 - a)\sigma_2}{2\sigma_1 a + (a + 2\lambda\sigma_1)\sigma_2};\ E_0 = \frac{J}{\sigma_1} \end{aligned} \qquad (8)$$

In writing the relation for the moment M in equation 8, we have introduced a new term χ, the Polarizability. Note that the units of polarizability are length cubed. To the extent that the transverse impedance parameter χ is complex, the polarizability is also complex.

Metallic objects have a high conductivity ($\sigma_2 > 10^7$ S), while the background medium is water

that generally has a conductivity range of $10^{-2} < \sigma_1 < 10$ S. Hence the ratio σ_1/σ_2 is very small ($\sigma_1/\sigma_2 < 10^{-6}$). To a good approximation, therefore, we can simplify the relation for polarizability χ in equation 8 to read

$$\chi \cong 4\pi a^3 \frac{1-\frac{\lambda\sigma_1}{a}}{2\frac{\lambda\sigma_1}{a}+1} = 3V \frac{1-\frac{\lambda\sigma_1}{a}}{2\frac{\lambda\sigma_1}{a}+1}; \quad V = \frac{4}{3}\pi a^3 = \text{Target Volume} \tag{9}$$

In the simplified version of the object polarizability (equation 9), we see that when the transverse impedance (λ) is zero, the polarizability is a real constant ($-4\pi a^3 = -3V$) proportional to the target volume (V) of the target. When we multiply the polarizability by the applied electric field, (E_0), we generate a dipole moment. From this moment, it is easy to estimate an anomalous voltage or electric field at any distance from the target using the relation

$$\delta\phi_e = \frac{M}{4\pi}\frac{\cos\theta}{R^2} \tag{10}$$

The Transverse Impedance (λ)

We have alluded to the fact that the transverse impedance parameter embodies the nature of the IP phenomenon. For the mechanism of electrode polarization, an inverse relationship between electrode polarization and frequency has been noted. At a single frequency, one can approximate the impedance by assuming that it is capacitive in nature. But over a broadband, the impedance varies inversely as a fractional power of frequency.

In this section, we examine the behavior of the polarizability under two assumptions:

1. A capacitive impedance layer - $\lambda = r_T + \frac{1}{j\omega C_l}$; r_T = transverse resistance *(11a)*

2. A Warburg impedance layer - $\lambda = r_T + \frac{K}{(j\omega)^{\frac{1}{2}}}$; $\frac{K}{(j\omega)^{\frac{1}{2}}}$ = Warburg impedance *(11b)*

Capacitive Impedance Layer - At low frequencies, we assume that the electrode impedance consists only of the Faradaic path shown in Figure 2.01. We further assume that the reactive part of the transverse impedance is capacitive in nature. That is, its impedance varies inversely with frequency. Substituting equation 11a into the simplified relation for polarizability (equation 9) yields the expression

$$\chi_c(\omega) = 3V \frac{1 + j\omega r_T C_l\left(1-\frac{a}{r_T\sigma_1}\right)}{2 + j\omega r_T C_l\left(2+\frac{a}{r_T\sigma_1}\right)} = 3V \frac{1 + j\omega\tau\left(1-\frac{a}{r_T\sigma_1}\right)}{2 + j\omega\tau\left(2+\frac{a}{r_T\sigma_1}\right)}; \ \tau = r_T C_l \tag{12}$$

Under this assumption, the frequency behavior of the target polarizability as indicated by equation 12 is that of a simple pole.

For practical reasons, we chose to measure the IP response in the time domain by observing its transient behavior after a "step-off" current pulse (similar to a conventional TEM pulse). The

step-off IP transient can be found from (12) by performing the inverse Laplace Transform of the product of (12) with the Laplace transform of a step-off current pulse to yield a relation for the step response transient behavior of the IP phenomenon

$$\chi_c(t) = \frac{2 - \frac{1}{2}\left(\frac{a}{r_T\sigma_1}\right)}{2 + \frac{a}{r_T\sigma_1}} e^{-\left(\frac{2}{2+\frac{a}{r_T\sigma_1}}\right)\frac{t}{\tau}} = \frac{2 - \frac{1}{2}\xi}{2+\xi} e^{-\left(\frac{2}{2+\xi}\right)\frac{t}{\tau}} \qquad (13)$$

Equation 13 shows that the target behavior is characterized by two parameters, τ (a time constant), and $\xi = a/(r_T\sigma_1)$ (a dimensionless ratio involving a characteristic target dimension, the transverse electrode resistance, and the conductivity of the medium). Figure 2.04 is a parametric plot that illustrates the transient behavior as a parametric function of parameter ξ. Note that polarization decreases and the effective time constant increases as the value of ξ increases. The polarizability is 0 for $\xi=4$, and is negative for values $\xi>4$. The parameter ξ involves both the transverse electrode resistance and the solution conductivity. Given a constant target dimension (a), if one or both of these values decrease, the result is to increase ξ. Thus, one might expect that the IP response would decrease as the water medium goes from salt water (higher σ_1) to freshwater. As we indicate later in this report, there is a decrease in the amplitude of the IP response from salt water to fresh water.

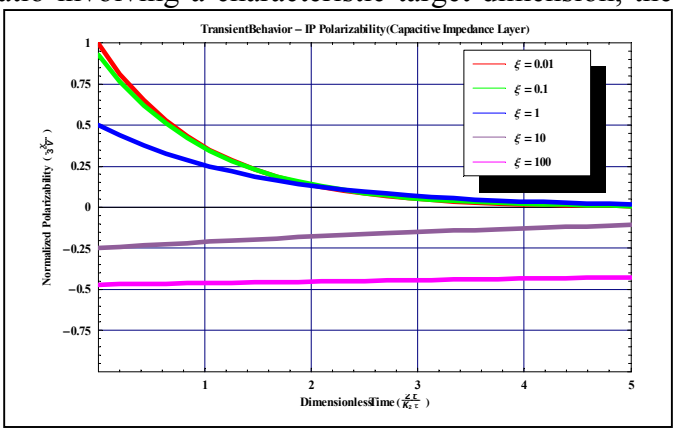

Figure 2.04: Parametric plot showing relative time-domain IP polarizability as a function of time with ξ as the parameter. The results are based on a capacitive model of Faradaic electrode impedance.

The Warburg Impedance Layer – In an approach exactly parallel to the previous section, we can develop relations for the frequency and time behavior of the target polarizability when the transverse impedance (λ) is characterized by the more complex Warburg impedance element. Upon substitution of equation 11b into equation 9 and simplifying a bit, we get the relation

$$\chi_W(\omega) = 3V \frac{1 + (j\omega)^{\frac{1}{2}}\left(\frac{r_T}{K}\right)\left(1 - \frac{a}{r_T\sigma_1}\right)}{2 + (j\omega)^{\frac{1}{2}}\left(\frac{r_T}{K}\right)\left(2 + \frac{a}{r_T\sigma_1}\right)} = 3V \frac{1 + (j\omega\tau)^{\frac{1}{2}}(1-\xi)}{2 + (j\omega\tau)^{\frac{1}{2}}(2+\xi)}; \quad \tau^{\frac{1}{2}} = \frac{r_T}{K} \qquad (14)$$

Unfortunately, we were not able to find the analytic Laplace transform for the step response corresponding to equation 14 for arbitrary values of the parameter ξ. However, we were successful in finding an analytic function of time for the special case ($\xi=0$). We give that expression in equation 15.

$$\chi_W(t)\Big|_{\xi=0} = (3V)\, e^{\frac{t}{\tau}} \left(1 - Erf\left[\left(\frac{t}{\tau} \right)^{\frac{1}{2}} \right] + Erfc\left[\left(\frac{t}{\tau} \right)^{\frac{1}{2}} \right] \right). \qquad (15)$$

where the terms Erf[], and Erfc[] denote the standard and complementary error functions as defined, for example, in Abromowitz and Stegun (6.5.16 & 6.5.17)[11]. We show a plot of the time behavior of equation 15 in Figure 2.05.

Although we were unsuccessful in deriving a general form for the TD step response of the polarizability function valid for all ξ, nonetheless we believe the general behavior of these decay curves as a function of ξ is the same as that shown in Figure 2.04. That is, the amplitude will decrease and the time constant will increase with increasing ξ.

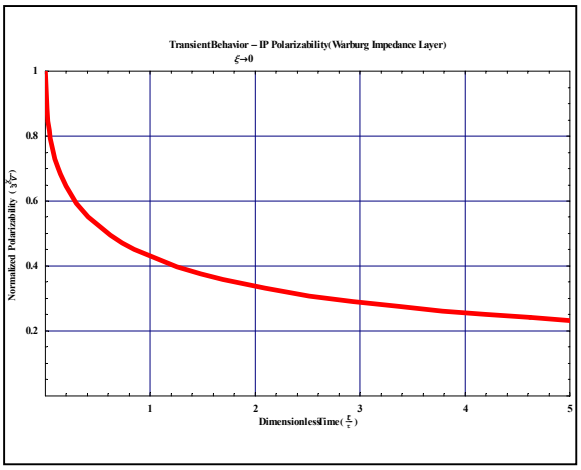

Figure 2.05: Parametric plot showing relative time-domain IP polarizability as a function of time with ξ=0. The results are based on a Warburg model of Faradaic electrode impedance

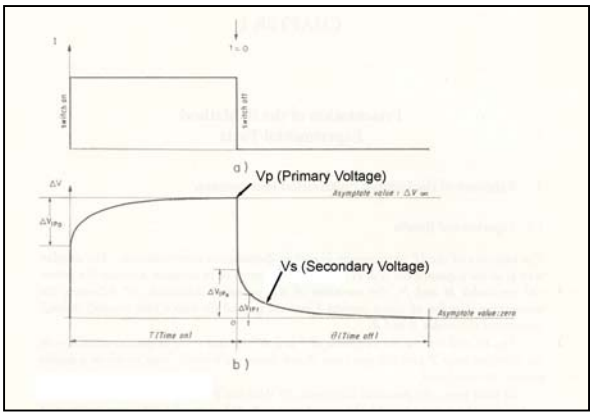

Figure 2.06: Schematic depiction of the IP phenomenon as seen in the time domain. (adapted from Bertin and Loeb [2])

2.2 Practical IP Measurements

We have shown in the previous section that the IP phenomenon is manifest in the frequency domain as a frequency dependent change in the resistivity. In point of fact, we must consider the resistivity to be a complex function of frequency. Historically, the IP phenomenon was observed by Conrad Schlumberger when he noticed that the potential voltage that he was observing did not immediately drop to zero after the interruption of the transmitted current when his receiver electrodes were located near a buried iron pipe [12]. This is the manifestation of IP in the time domain. In this section, we briefly discuss modern time domain and frequency domain IP measurements. We refer the reader to more complete discussions of IP measurement techniques and parameters to discussions by Sumner [3] and Bertin and Loeb [2].

2.2.1. Time Domain IP Measurements

The earliest measurements of the IP effect were made in the time domain. Following the interruption of the flow of a DC current, one measures and reports the decay of the secondary voltage that remains. Modern time domain IP instruments sample the secondary voltage, in one or more time gates or windows after the current shutoff. In addition, the instruments measure the primary voltage (V_p in Figure 2.06) just prior to the current shut-off.

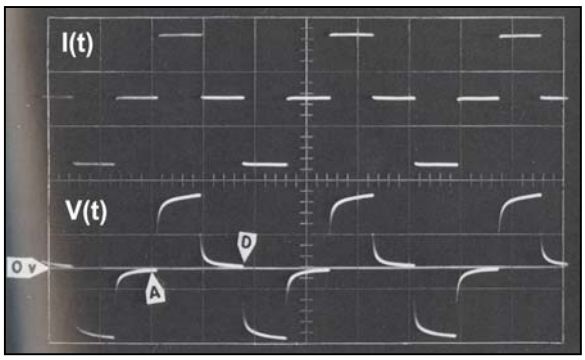

Figure 2.07: Oscillographs showing current waveform (top) and voltage waveform (bottom) for time domain IP. (after Sumner, [3])

The Newmont Mining Company was a pioneer in the development of the IP method. Newmont designed a portable time domain IP receiver for mineral exploration. That receiver integrated the secondary voltage (V_s) falling within a single time gate in a 0.125Hz 50% duty cycle waveform. They defined a chargeability parameter (the Newmont M parameter) that has since become something of standard parameter measured and reported in many time domain IP receivers. A good explanation of the M parameter was published by Swift [1]. The Zonge algorithm for computing chargeability is consistent with the definition provided in Swift's paper. Note that the M parameter is defined for a base period of 8 seconds. However, the Zonge GDP-32^{II} receiver is able to collect IP data using a selectable base frequency and their standard definition of the M parameter simply scales the window width according to the base period (T) that is selected. The standard Zonge definition for the chargeability parameter is

$$\mathbf{M} = \frac{1.87}{V_p}\int_{0.45\left(\frac{T}{8}\right)}^{1.1\left(\frac{T}{8}\right)} V_s(t)\,dt \text{ ; where } T \text{ is the base period (seconds)} \qquad (16)$$

In equation 16, we see that when the period is 8 seconds the value of M agrees with the definition shown in Figure 2.08. However, at higher base frequencies (small periods T) there is a problem with this definition. To understand the problem, assume that the secondary potential is constant. In this case, we can integrate equation 16 to get the relation

$$\mathbf{M} = \left(650\frac{T}{8}\right)\left(\frac{\bar{V}_s}{V_p}\right);$$

T = Period corresponding to base frequency (in seconds)

650 = Window width expressed in milliseconds for $T = 8s$ *(17)*

$\bar{V}_s$ = Assumed constant secondary voltage

V_p = Primary voltage immediately before turn-off

$\mathbf{M}$ = Chargeability expressed in milliseconds

The problem can be seen in equation 17 where the chargeability is multiplied by the factor (T/8). As we increase base frequency (decrease T), the computed chargeability decreases simply because the original definition for M in Figure 2.08 was scaled. This problem has resulted in considerable discussion about whether or not to change the definition of the "Zonge" standard chargeability to eliminate the scaling problem when we measure IP at higher frequencies.[3] For the Mare Island experiments, we redefined the relation for chargeability in the Zonge receiver to eliminate the artificial reduction in chargeability with increasing base frequency by multiplying equation 16 by the factor (8/T). The modified definition becomes

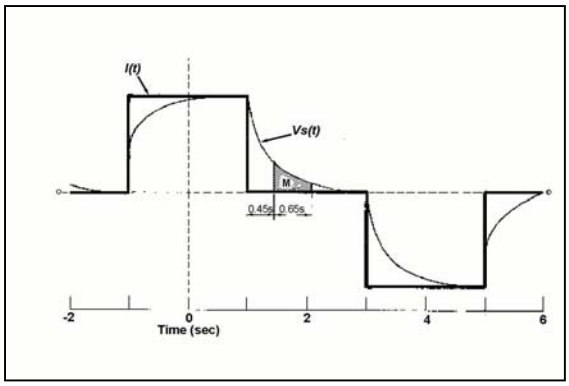

Figure 2.08: Definition of the Newmont M parameter (adapted from Swift [1]).

$$\mathbf{M}_1 = \left(\frac{1.87}{V_p}\right)\left(\frac{8}{T}\right)\int_{0.45\left(\frac{T}{8}\right)}^{1.1\left(\frac{T}{8}\right)} V_s(t)\,dt\ ;$$

T is the base period (seconds) *(18)*

$\mathbf{M}_1$ = Scaled chargeability parameter used at MINS

From equation 8, note that the IP polarizability parameter χ can be obtained from a knowledge of the targets dipole moment M and the polarizing electric field E_0 according to the relation

$$\chi = \frac{M}{E_0} \qquad (19)$$

Now, the object's dipole moment (M) gives rise to the secondary voltage, while the polarizing electric field (E_0) controls the value of the primary voltage (V_p). The chargeability M as defined

[3] Until relatively recently, Zonge never measured time domain IP chargeability at any frequency other than 0.125. Several years ago, however, they began using a base period of 0.5Hz for high resolution surface tomography measurements. The problem was identified at that time and it was decided to keep the eqn 16 definition for purposes of continuity. However, for this marine work, we planned to use a frequency of 8 Hz. This means that the chargeability as defined by equation 16 is effectively divided by 64 as compared with what would be measured at 0.125Hz.

either by equations 16 or 18 is in fact a ratio of the two voltages (i.e. V_s'/V_p) and therefore it is, in fact a direct measure of the polarizability constant for the target.

2.2.2. Frequency Domain IP Measurements

Modern frequency domain instruments, such as the Zonge GDP-32^{II} measure the complex frequency response of a transmitted periodic waveform as amplitude/phase or inphase/quadrature measurements as a function of frequency. This method is often referred to as the Complex Resistivity method. The usual transmitted current waveform is a square wave such as that shown in Figure 2.09 (top). A typical received voltage waveform exhibiting IP corresponding to the square wave transmitter current waveform is pictured as the bottom waveform in Figure 2.09.

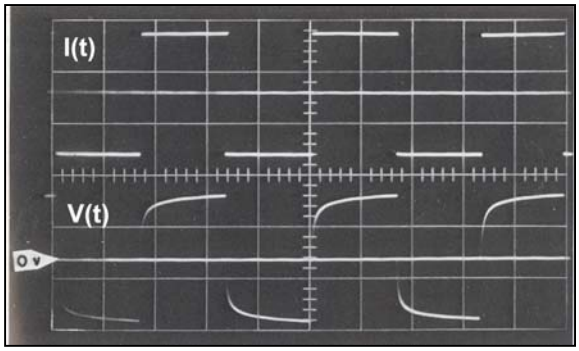

Figure 2.09: Typical current and voltage waveforms for a frequency domain IP measurement.

The quadrature voltage (V_Q) at any given frequency is the voltage that results from the discharge of the polarized target moment (M). Likewise, the inphase voltage (V_I) is the voltage related to the polarizing field (E_0). Therefore, the ratio of these two voltages are related to the polarizability (χ). Thus we can infer the relationship

$$\chi = \frac{M}{E_0} = C\frac{V_Q}{V_I} = Tan(\phi) \approx \phi \qquad (20)$$

where C is a constant and ϕ is the phase.

2.3 Interfering Responses

There are other mechanisms that can produce a transient or complex frequency response when measured with an IP receiver. For the purposes of UXO detection, these mechanisms can be considered to generate interference. In this section we discuss two important sources of (possibly) interfering responses

2.3.1. Membrane Polarization

Porous material containing small amounts of clay minerals composed of platy silicates can significantly reduce the mobility of the cations in the saturating fluids due to the specific cation exchange capacity of the material. When current is passed through such a material, a polarization occurs which takes time to decay. Membrane polarization is an important mechanism for mining and groundwater applications. It is also used in petroleum formation evaluation to help estimate the "shale" content in reservoir sands. IP response arising from small amounts of clay in the sub-bottom should manifest itself as a very slowly varying "background" response and therefore will be easily handled by standard background removal techniques.

2.3.2. Electromagnetic Coupling

Because we transmit a time-varying current into the ground or, in this case the water, we must consider the possibility that there will be measureable voltages between our receiver electrodes

caused by eddy currents induced in earth or sea water. The theory for the electromagnetic coupling or mutual inductance of grounded wire is treated in detail by Sunde [13] and also by Ward and Hohmann [14]. We have calculated the theoretical coupling for a uniform half-space using the gradient (Schlumberger) array geometry (10m AB, 1m MN) and a dipole-dipole array (2m dipole, n=4). We used the gradient array at Mare Island.[4] We show the results of our numerical calculation in Figures 2.10a (Frequency Domain), and Figure 2.10b (Time Domain) for two arrays.

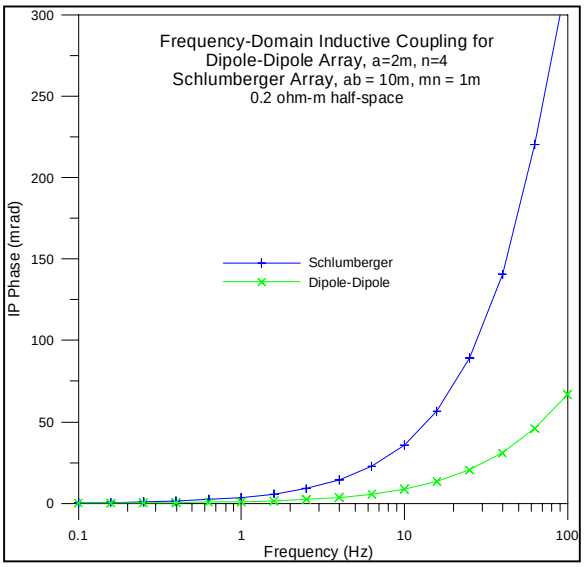

Figure 2.10a:
Electromagnetic coupling – Frequency Domain

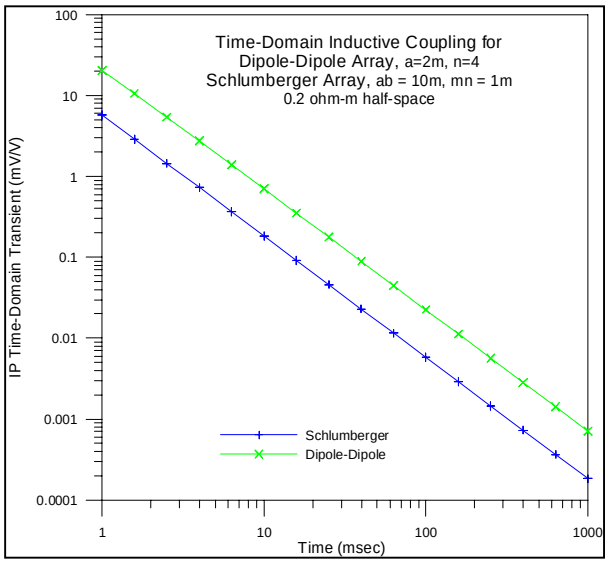

Figure 2.10b:
Electromagnetic coupling – Time Domain.

The phase shift as a function of frequency becomes significant for both arrays at frequencies above 1Hz. Therefore, if we were to acquire frequency domain data at 8 Hz, we would expect that there would be a significant background response. It is notable that in the frequency domain, the coupling in the dipole-dipole array is much smaller than that for the Schlumberger (Gradient) array. It is also noteworthy that the coupling response is directly proportional to the product of the lengths of the transmitter and receiver dipole. Thus, for the Schlumberger array (blue curves in Figure 2.10), that product would be (AB*MN). This means when we change the geometric scale of the array, the coupling increases/decreases by the square of the scale factor. In Figures 2.10, for example, we calculated gradient array coupling for AB=10m and MN=1m. However, much of our data were acquired with an AB=5m and an MN=½ m (i.e., a scale factor of 0.5). Therefore, we can estimate the coupling for this smaller array size by multiplying the results shown in Figures 2.10 by 0.25 (i.e., 0.5^2). Not shown in Figure 2.10a is the sign of the phase response of EM coupling for the two arrays. It is significant that for the Schlumberger array, the phase is opposite in sign to phases arising from IP targets (destructive interference) while for the dipole-dipole array, the phase has the same sign as a normal IP response.[5] Likewise, the time domain transients for the two arrays have opposite signs.

---

[4] See Figure 3.17 for diagrams of various electrode arrays.

[5] As observed, IP phase responses are normally negative (i.e., realizable linear system). But by convention, the sign is inverted so that the reported numbers are positive.

In Figure 2.10b, we show the computed time-domain transients for the EM coupling of the two arrays. These transients are log-log linear indicating that they have a power law decay $t^{-3/2}$. This should come as no surprise to those readers familiar with the behavior of electromagnetic fields over a uniform half-space. Inductive effects are less than 1 mV/V by 10 msec. As we stated above, time-domain inductive signal strength is proportional to product of the transmitter and receiver electrode dipole lengths so the Schlumberger array inductive signal at a given time is greater than the dipole-dipole signal. However, the time-domain transient is normalized by peak voltage, so normalized inductive effects are lower for the Schlumberger array than for the dipole-dipole array.

We used the transients shown in Figure 2.10b to calculate the amplitude of the scaled chargeability parameter M_1 (equation 18), in order to estimate the level of the EM coupling interference as a function of base frequency (f = 1/T). Those results are shown in Figure 2.11, showing that EM coupling in the time domain at base frequencies of 8Hz and even higher is negligible.

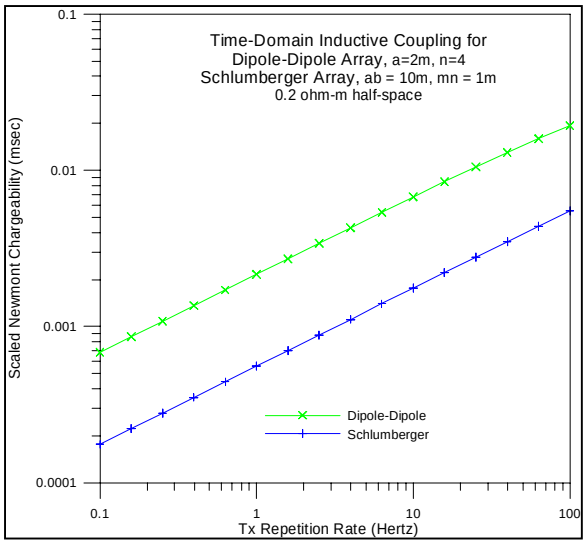

Figure 2.11: Time domain EM coupling as measured by the scaled chargeability parameter (M_1) as a function of repetition rate (i.e., *1/T*)

3. Preliminary Study

As we have indicated in the introduction, the evidence for a measurable IP response associated with large metallic objects such as UXO is anecdotal. The early work on the IP method conducted at the Naval Ordnance Laboratory has apparently been lost. All that remains is the testimony of one or two individuals who were involved with the project. As mining geophysicists, we have on occasion identified possible "cultural" IP responses associated with buried metallic objects such as fence posts and water pipes. So it is natural that we believe that IP can, in principle, be used to detect metallic objects of interest.

To re-establish that IP is indeed associated with isolated metallic objects submerged in water, to determine the magnitude of these effects, and to study the effect of water salinity, we have conducted scale-model tests of the IP method in the laboratory using fresh and salt water. The results of these laboratory tests provided a useful datum with which MPT, LLC (Reno, NV) was able to use in furthering the model study using numerical methods. The primary objective of the numerical modeling was to select an optimal array for deployment during the full-scale experiment.

In order to meet the challenge of modeling the IP effect of small isolated targets in salt water, we found it necessary to use principles developed to describe the IP effect at individual grain boundaries. Layered models with an optimized resistive shell were developed to match scale model IP results. We calibrated our numerical modeling to the laboratory-measured IP response, then pursued the array optimization studies. While the IP response was strongest in salt water and at low frequencies, the strength of the primary field is of significant concern in salt water where it is orders of magnitude less than in fresh water or on the ground. In this paper, we report the results of our numerical models and demonstrate that the calibrated responses match scale and field models. We have developed a 'bead' plot that compares primary field strength with IP effect to aid in selection of optimal arrays. Our studies also investigated target size in relation to receiver dipole length. Targets smaller than half a receiver dipole produce low amplitude, complex signals.

3.1 Laboratory Scale-Modeling

To study the magnitude and broadband behavior of IP associated with metallic objects we assembled a laboratory-scale model apparatus using a 7-gallon aquarium. A photograph of the aquarium is shown in Figure 3.01. We placed current electrodes at each end of the aquarium so that when energized, an approximately uniform current density flows through the solution.[6] A layer of glass beads (100-170 sieve) was placed in the bottom of the tank. Our experiments were conducted using water at two salinities:

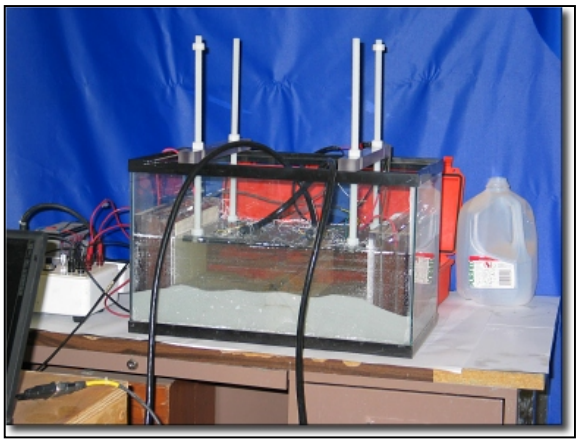

Figure 3.01: Photograph of aquarium used in scale-model experiments.

[6] All measurements were made with a current of 10ma. The approximate current density was about 24μA/cm^2 in the water and approximately 12μA/cm^2 for the current passing through the saturated glass beads.

1. Tucson Tap Water (ρ = 26 Ω-m @ 25˚C)
2. 30,000ppm NaCl (ρ = 0.236 Ω-m @ 25˚C)

Potentials were measured on the water surface with a grid of 30 12mm Ag-AgCl disk electrodes (In Vivo Metric, Ukiah, CA; Type 204). Potential electrodes were organized as 5 rows and 6 columns on a 4cm grid interval. Figure 3.02 shows a cross-section of the aquarium pictured in Figure 3.01. The target was a rusty 3-in-diameter steel crushing mill ball, supported by a 1-in diameter PVC cylinder, presenting a so-called "proud" target on the surface of the glass beads.

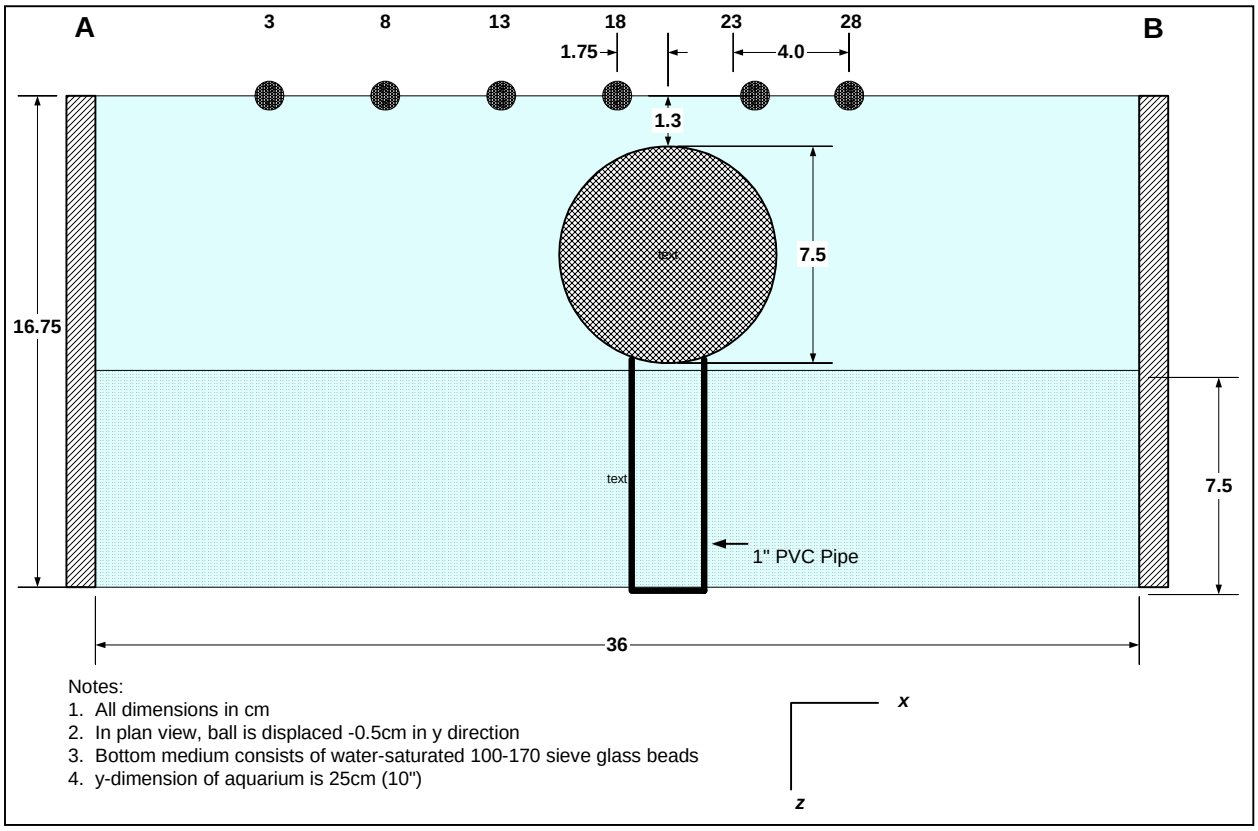

Figure 3.02: Center-line cross-section through model tank. The figure shows the approximate position of the 3" target during measurements.

The objective of these measurements was primarily to establish the magnitude and spatial variation of the IP response over the target. We connected the receiver electrode grid to a Zonge MX-30 electrode multiplexer. The MX-30 was developed to facilitate electrical impedance tomography (EIT) measurements. In this case, the multiplexer was used to gather data simulating the acquisition of measurement profiles over the target area. A profile measurement consisted of the measurement of the potential difference between a pair of adjacent electrodes (i.e., a 4cm electric dipole measurement) along one of the 5 electrode rows.

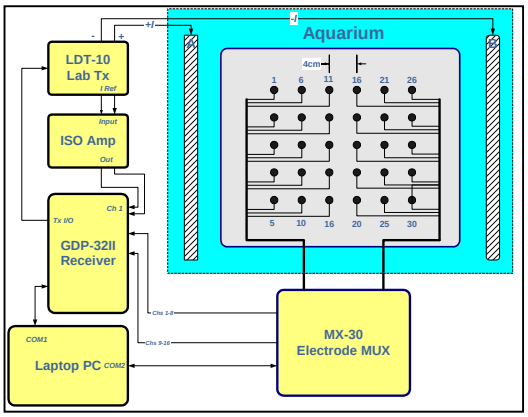

Figure 3.03: Functional block diagram of scale model acquisition system.

Under the control of a laptop PC, we were able to acquire a total of 25 dipole measurements over the target with multi-channel receiver (8 channels) in less than 15 minutes. Figure 3.03 contains a simplified block diagram of the experimental apparatus. It also contains a plan view of the electrode grid corresponding to the cross-section shown in Figure 3.02.

3.1.1. Laboratory Procedure

We measured background resistivity and IP response before placing the target in the tank. After we measured the background, we placed the target in the tank and allowed it to equilibrate with the medium for a minimum of 48 hrs before we measured the response of the target. For each target situation (i.e., background/3-in steel sphere), we acquired 3 types of data as follows:

1. **Time Domain IP Chargeability (M):** We acquired single-gate "Newmont" charge-ability over the 25 longitudinal dipoles (4 cm spacing) that are available on the 5x6 electrode grid.
2. **Time Domain IP Chargeability (M+13 windows):** We acquired 13-gate IP transient data over the 5 dipoles comprising the central profile over the target.
3. **Frequency-Domain Complex Resistivity Measurements:** We acquired broadband complex resistivity measurements at 15 frequencies covering the frequency range $0.125 \leq f \leq 72$ Hz. As with the 13-gate IP transient data, these data were acquired for the 5 dipoles along the central profile over the target.

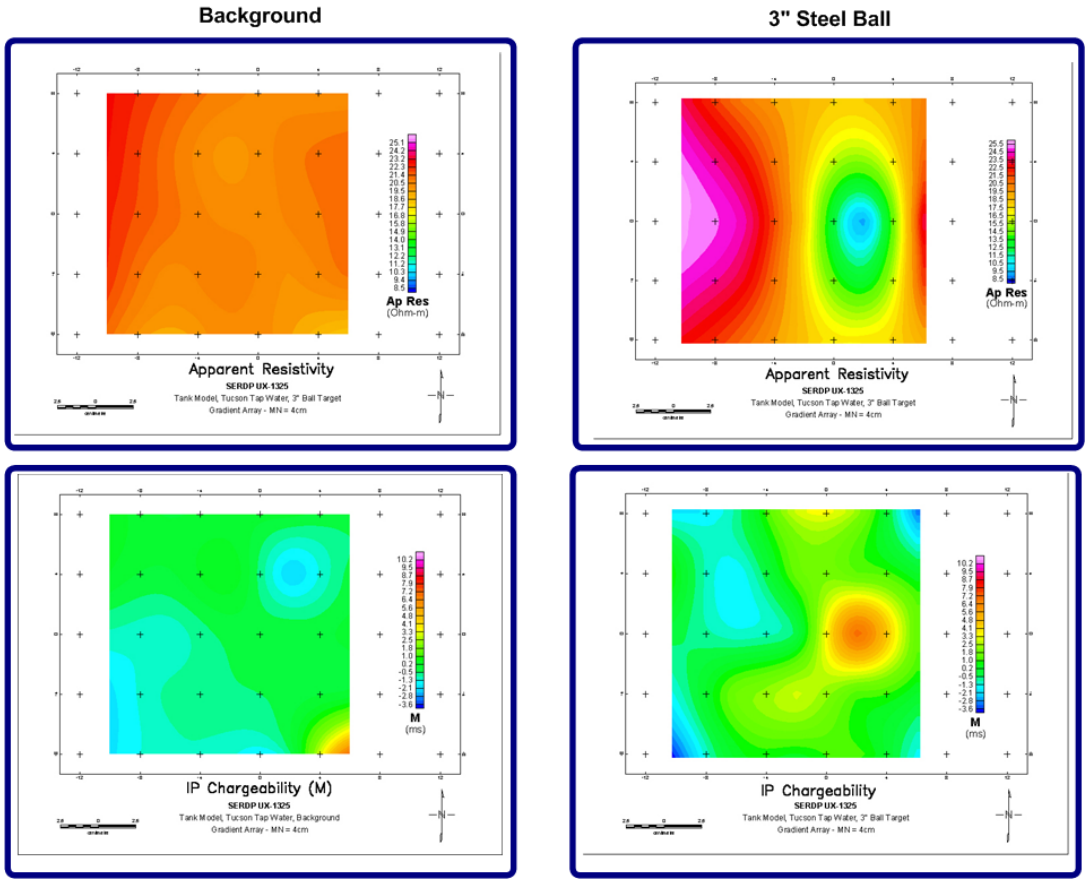

Figure 3.04: Summary plot showing apparent resistivity and IP chargeability for background and 3" steel ball target in Tucson tap water (ρ=26 Ω-m)

3.1.2. Results [Tucson Tap Water]

Results for the mapping experiment are summarized in map form in Figure 3.04. In freshwater, we were able to measure a peak IP anomaly of approximately 8 ms directly over the target against a background response of less than 1 ms. The resistivity dropped from a background of approximately 21 Ω-m down to a low of about 9 Ω-m – a change of 2:1, more or less. The IP anomaly is not large. However, even at this low level, it is very mappable provided the electrodes are close enough to detect the signal.[7] But it is clear that the signal would probably be undetectable at a distance of 5 or 6 cm.

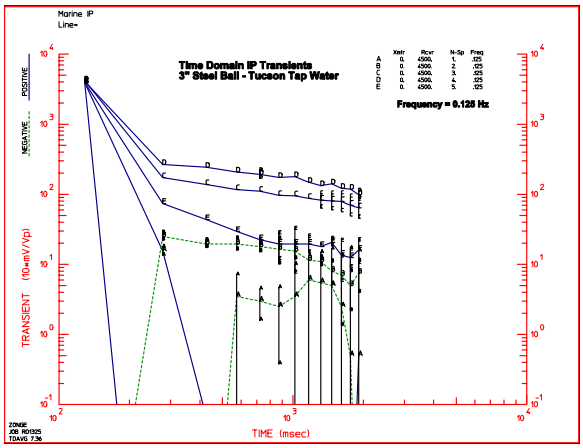

Figure 3.05: IP decay transients measured over the central profile for a 3" steel ball in Tucson tap water.

In Figure 3.05, we show the time-domain response of five 4-cm dipoles along the central profile (row 3) of the electrode matrix. For example, the curve marked 'D' corresponds to the dipole comprised of electrode pair (18,23) (See Figure 3.03 for electrode numbering convention). Note that the first two dipoles (i.e., (3,8) and (8,13)) measure a negative IP effect. The strong positive value in the earliest time gate is an instrument effect and should be ignored. When the IP transient is strong enough to measure with low noise (curves "C" and "D"), the decay is rather log-log linear suggesting a decay proportional to $t^{-0.39}$.

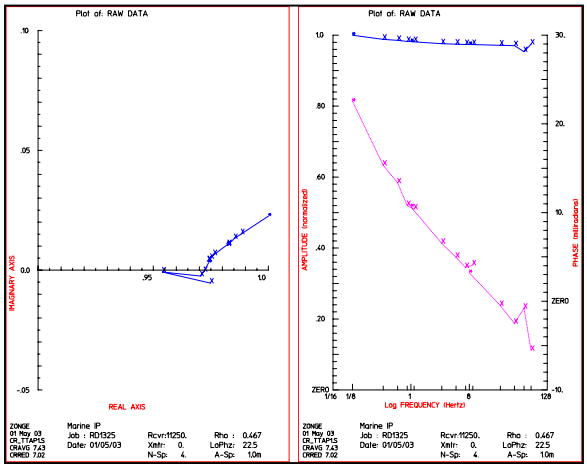

Figure 3.06. Complex resistivity (CR) spectrum corresponding to a dipole centered over a 3" steel sphere immersed in Tucson tap water.

In Figure 3.06, we show the complex resistivity spectrum for the dipole center dipole ('D' in Figure 3.05). The panel on the left hand diagram is an Argand diagram showing the behavior of the normalized real and imaginary parts of the spectrum. The right hand panel shows the behavior of the amplitude and phase of the response. The blue curve (amplitude) has been normalized to a value of 1 at the lowest frequency (0.125 Hz). The curve shows that there is a small decrease in amplitude with frequency. The percentage change in amplitude at two different frequencies was an early frequency domain measure of IP.[8] The phase, measured in milliradians (~17 mr/deg) is a more modern measure of

---

[7] Fluid levels varied as the water in the aquarium evaporated. All measurements over the ball were made with approximately 1.5 cm of water over the top of the ball.

[8] The percent frequency effect is usually defined as $PFE = 100\dfrac{V(f_1) - V(f_2)}{V(f_1)}$ where V signifies the voltage amplitude measured at frequency *f*.

IP response. The spectrum shows that the IP phase decreases rapidly with increasing frequency. At 8 Hz, a frequency that might be useful for continuous measurements, the peak phase of the anomaly for the 3" steel ball is only 4 or 5 mr. Thus the frequency domain measurements of the peak IP response over the ball target are entirely consistent with the time domain measurements in Figure 2.4 where the peak time domain chargeability was only 6-7 ms.

3.1.3. Results [30,000 ppm NaCl]

To test the effect of salinity on the IP response, we repeated the previous measurements using a solution of 30,000 ppm NaCl. We show the maps corresponding to apparent resistivity and chargeability in Figure 3.07. As with the tap water case, the resistivity shows a small decrease over the target (a change of only about 15%). More notable, however, is that the chargeability peak is now above 100 ms. Although these experiments need to be repeated with targets with different compositions, we have concluded on the basis of this work that the IP effect in sea water will be significantly stronger than it would for the same target immersed in freshwater.

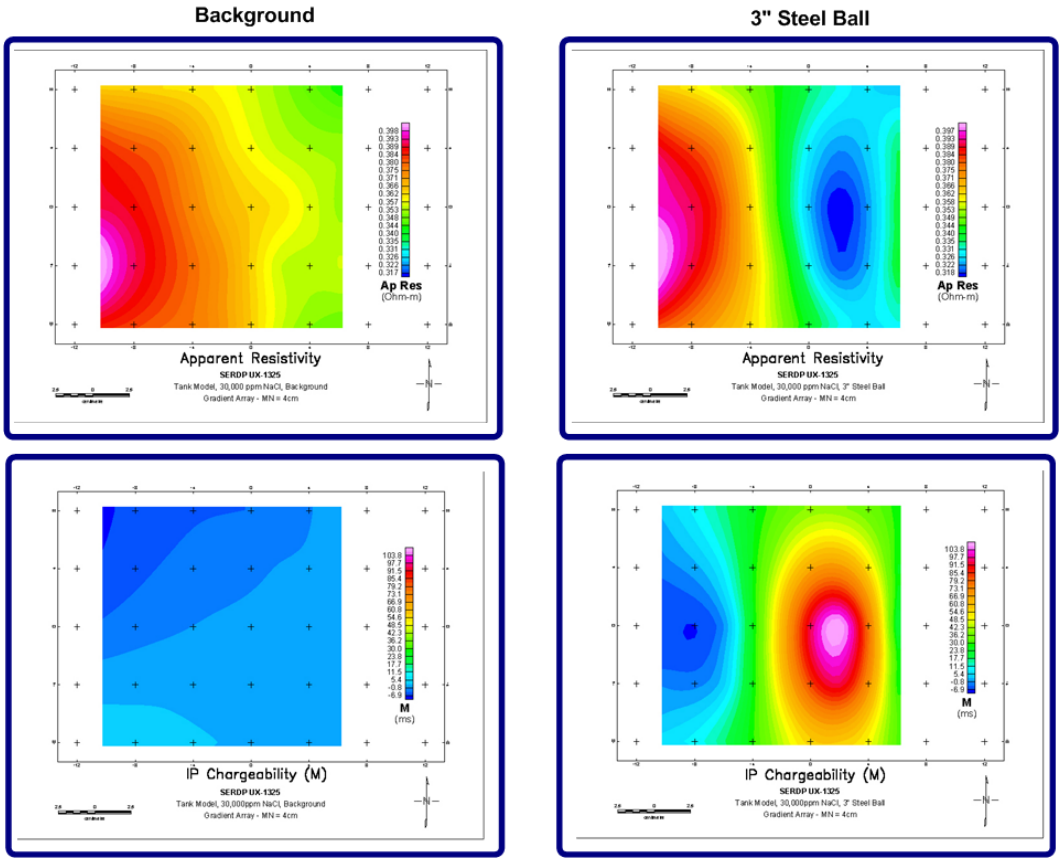

Figure 3.07: Summary plot showing apparent resistivity and IP chargeability for background and 3" steel ball target immersed in a solution of 30,000 ppm NaCl (ρ=0.236 Ω-m).

The decay curves and complex resistivity spectrum for the salt water experiment are provided in Figure 3.08. As with the tap water results shown in Figure 3.05, the corresponding results for the salt water solution (Figure 3.08a) show a similar inverse power law decay with time. In this case, the exponent is slightly larger ($t^{-0.57}$). Because of the larger IP response, the negative IP effects seen on the first two dipoles (curves 'A' and 'B') in Figure 3.05) are not as noisy in the salt water case. Moreover, the decay curve shape remains constant from the negative lobe

(curves ‘A’, ‘B’ in Figure 3.08a) of the anomaly to the positive lobe (curves ‘C’, ’D’, ‘E’).

In Figure 3.08b, we show the complex resistivity spectrum for the dipole that is almost directly over the target. Note that the phases at low frequencies are well over 100mr. At a frequency of 8 Hz, the likely frequency for towed-array measurements, the phase response remains close to 50mr. The scale model results provided in Figures 3.05, 3.06, and 3.08 unambiguously indicate that we can expect the IP responses from single metal objects, however they are measured, to be approximately 5 times larger when measured in salt water than when measured in fresh water.

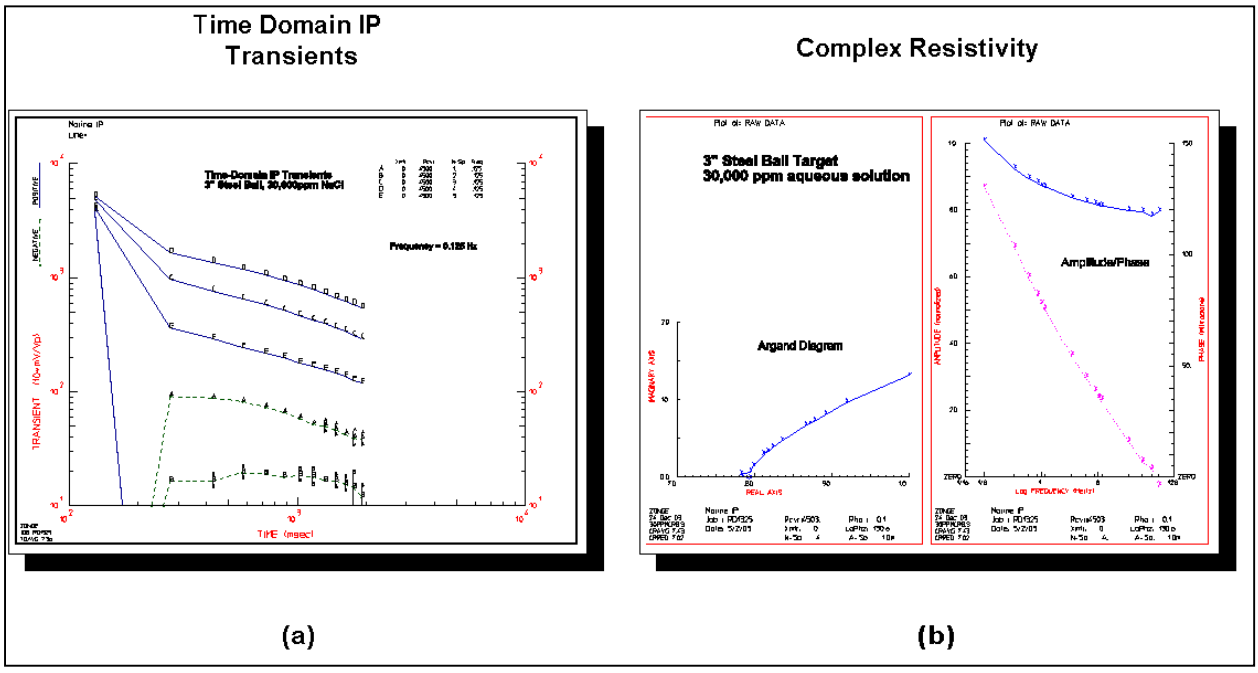

Figure 3.08: IP transients and complex frequency spectra acquired over a 3” steel ball immersed in an aqueous solution of 30,000 ppm NaCl. The 5 transients in (a) represent the 5 dipoles in the center-line profile over the target. The complex resistivity spectrum was measured using electrode numbers (18,23).

3.1.4. Discussion

The maps of both the resistivity and IP response over the target ball shown in Figures 3.04 and 3.07 leave no doubt that the target behaves as a dipole. It is easy, in particular, to fit the chargeability map in Figure 3.07 to a horizontal dipole located in the approximate position of the peak. The results of this fitting exercise are shown in Figure 3.09. The assumption is that the polarizing field is uniform.

The model results show that the conductive (salt water) medium enhances the amplitude of the response. This was an important finding because it suggested that we perform our full-scale tests in salt water in order to maximize the amplitude of the response. In salt water, these results demonstrate that the IP response may exceed 100ms in the time domain and 100mr in the frequency domain. On land, the practical noise floor of IP measurements is around 1ms/1mr and, therefore, we can expect better than 40dB of signal-to-noise when the measuring electrodes are directly over practically on top of the target. The attenuation of this signal with target depth follows an inverse square law if we are dealing with potentials as in equation 7. However, better spatial resolution can be obtained by measuring the potential difference between two electrodes

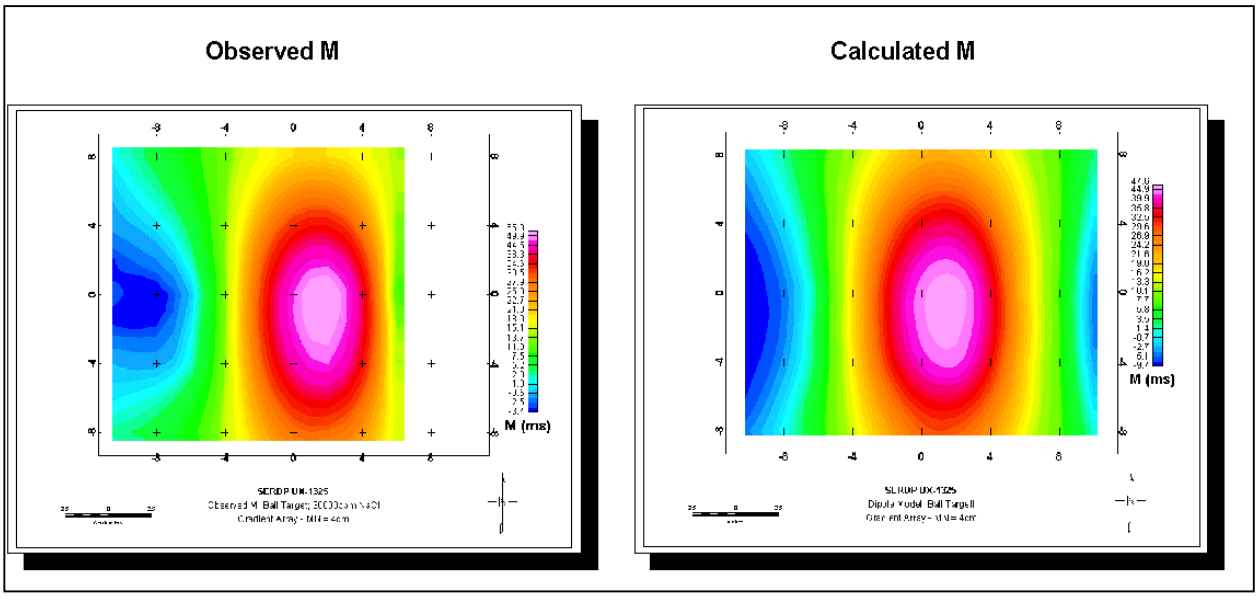

Figure 3.09: Observed and calculated chargeability for the 3" ball target in a 30,000 ppm NaCl solution. The model calculations assume a horizontal dipole.

spaced close together (i.e., a horizontal electric dipole). When the dipole spacing is small relative to the distance to the target, the potential difference is directly proportional to the horizontal electric field. Therefore, for electrode arrays with small dipoles as sensors, the attenuation of the signal with distance varies inversely as the cube of the distance to the target (i.e., $1/R^3$).

3.2 Numerical Model Study

In this section, we describe the numerical modeling effort that was conducted under subcontract to Zonge Engineering by MPT (Reno, NV) to assist in the design of a full-scale experiment. An important objective of the study was to find an optimal electrode array for detecting an object of a given size, depth, and aspect ratio. To meet that objective, we studied a number of electrode array geometries to determine their range of investigation both in depth and in lateral offset, and the relative magnitude of IP response. Our goal was to identify an array having the best possible depth and lateral range of investigation. A second objective was to determine whether these arrays can provide any sense of target aspect.

3.2.1. Modeling Considerations

Numerous authors have contributed to our understanding of the IP effect in mineralized rock [15], saturated rock [16], sulfides [17], layered earths [18, 19], and environmental mapping [20]. Numerical modeling methods have been developed [10, 21], and studies using these methods have been directed at comparing electrode arrangements [22] and examining depths of investigation [23]. However, the specific challenges of modeling the IP response of UXO in fresh and salt water have not previously been addressed. While our numerical modeling codes employ traditional off-time definitions for chargeability, we found that models of UXO targets had to be developed based on principles developed to describe the IP effect at individual grain boundaries. Similar to the sphere model with the transverse impedance boundary derived in section 2, we found that a layered sphere model consisting of a conductive core covered with a resistive shell with a high intrinsic IP effect was necessary in order to match scale model IP

results. The resistance of the shell has an optimal value that we established using trial and error methods. Array optimization studies were completed using models calibrated to this response.

3.2.2. Model Calibration

The response amplitudes from preliminary models were extremely low. The salt-water environment and isolated target present several challenges to the numerical models. The environment is extremely conductive and the target is a single chargeable entity. The modeling code was designed to represent distributed, homogenous IP effects. It was important to calibrate the model to a known physical model. For this purpose, we used the scale model work described earlier in this section.

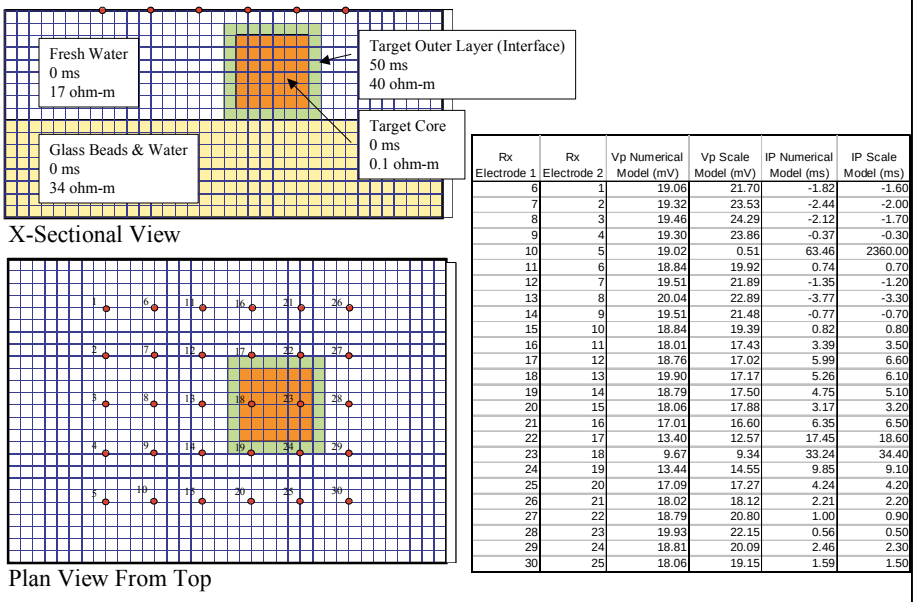

Rx Electrode 1	Rx Electrode 2	Vp Numerical Model (mV)	Vp Scale Model (mV)	IP Numerical Model (ms)	IP Scale Model (ms)
6	1	19.06	21.70	-1.82	-1.60
7	2	19.32	23.53	-2.44	-2.00
8	3	19.46	24.29	-2.12	-1.70
9	4	19.30	23.86	-0.37	-0.30
10	5	19.02	0.51	63.46	2360.00
11	6	18.84	19.92	0.74	0.70
12	7	19.51	21.89	-1.35	-1.20
13	8	20.04	22.89	-3.77	-3.30
14	9	19.51	21.48	-0.77	-0.70
15	10	18.84	19.39	0.82	0.80
16	11	18.01	17.43	3.39	3.50
17	12	18.76	17.02	5.99	6.60
18	13	19.90	17.17	5.26	6.10
19	14	18.79	17.50	4.75	5.10
20	15	18.06	17.88	3.17	3.20
21	16	17.01	16.60	6.35	6.50
22	17	13.40	12.57	17.45	18.60
23	18	9.67	9.34	33.24	34.40
24	19	13.44	14.55	9.85	9.10
25	20	17.09	17.27	4.24	4.20
26	21	18.02	18.12	2.21	2.20
27	22	18.79	20.80	1.00	0.90
28	23	19.93	22.15	0.56	0.50
29	24	18.81	20.09	2.46	2.30
30	25	18.06	19.15	1.59	1.50

Figure 3.10: Numerical model calibration to 3" steel ball model immersed in Tucson tap water (inhomogeneous target case).

The first data available were for the target in Tucson tap water. Figure 3.10 shows a relatively accurate representation of the ball as a conductive core and a resistive, chargeable outer layer constructed using 1 cm cells. This outer layer represents the surface impedance between the metal and electrolyte. This model provides a good data fit, generally fitting the data within 10%. We also developed a simpler, homogeneous-region model (see Figure 3.11). In this case, the sphere is replaced by a single cube with an intrinsic, but unrealistically high, resistivity of 6 Ohm-m and an intrinsic chargeability of 50 ms. The data fits are not as good as for the layered sphere, but were considered sufficient for comparing the responses of different arrays.

When data became available for the 3" ball immersed in an aqueous solution of 30,000 ppm NaCl, we derived a model for these data (Figure 3.12). These data were collected at 1/4 Hz. At this stage, the additional complication of higher frequencies was introduced. A minimum frequency of 8 Hz is necessary for any kind of practical towed marine array since this permits a navigational speed of 2-4 knots. One of the IP parameters measured by Zonge GDP-32[II] receiver is the Newmont chargeability "M"[1] (equation 16). As we indicated in section 2 of this report,

the extension of the definition of chargeability to other frequencies necessarily requires a scaling by the new frequency to 0.125 Hz. We observed that the required scaling results in the artificial reduction in the IP response by the factor (T/8) where T is the base period of the transmitted waveform.

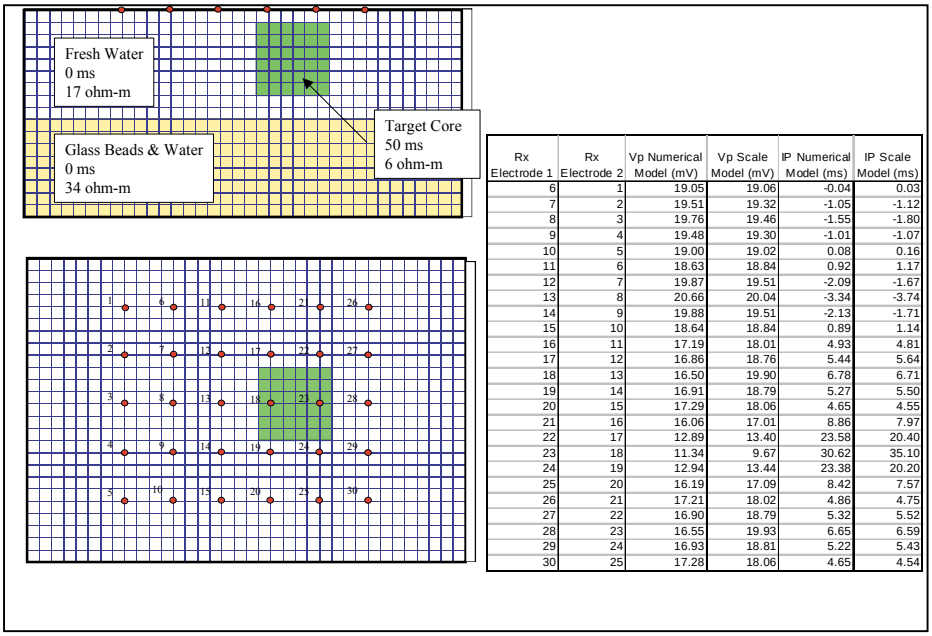

Rx Electrode 1	Rx Electrode 2	Vp Numerical Model (mV)	Vp Scale Model (mV)	IP Numerical Model (ms)	IP Scale Model (ms)
6	1	19.05	19.06	-0.04	0.03
7	2	19.51	19.32	-1.05	-1.12
8	3	19.76	19.46	-1.55	-1.80
9	4	19.48	19.30	-1.01	-1.07
10	5	19.00	19.02	0.08	0.16
11	6	18.63	18.84	0.92	1.17
12	7	19.87	19.51	-2.09	-1.67
13	8	20.66	20.04	-3.34	-3.74
14	9	19.88	19.51	-2.13	-1.71
15	10	18.64	18.84	0.89	1.14
16	11	17.19	18.01	4.93	4.81
17	12	16.86	18.76	5.44	5.64
18	13	16.50	19.90	6.78	6.71
19	14	16.91	18.79	5.27	5.50
20	15	17.29	18.06	4.65	4.55
21	16	16.06	17.01	8.86	7.97
22	17	12.89	13.40	23.58	20.40
23	18	11.34	9.67	30.62	35.10
24	19	12.94	13.44	23.38	20.20
25	20	16.19	17.09	8.42	7.57
26	21	17.21	18.02	4.86	4.75
27	22	16.90	18.79	5.32	5.52
28	23	16.55	19.93	6.65	6.59
29	24	16.93	18.81	5.22	5.43
30	25	17.28	18.06	4.65	4.54

Figure 3.11: : Numerical model calibration to 3" steel ball model immersed in Tucson tap water (homogeneous target case).

The chargeability M, defined in equation 16 and usually expressed in units of milliseconds (i.e., mV-sec/Volt), is essentially the average secondary voltage times the window width. This has implications for field data that would (ideally) be collected at 8 Hz. However for the array comparison study we decided to standardize on a frequency of 1/8 Hz (effectively making T=8 for all frequencies in 15 above). Our modeling programs calculate IP response as the ratio of received secondary voltage to the primary voltage (V_s/V_p) and consequently we chose to use the measurement parameter (mV/V) or mr as the basis for our comparisons. As we can see from Figures 3.06 and 3.08, IP responses for the ball target vary slowly with delay time. The log-log decay curves indicate power law attenuation of the IP decay curve, respectively of $t^{-0.39}$ for Tucson tap water, and $t^{-0.57}$ for the target in 30,000 ppm NaCl. To affect our comparison, therefore, we converted Zonge chargeabilities measured at ¼ Hz to an estimate of IP in units of mV/V at 1/8 Hz by multiplying Zonge values by a factor of 2.3 to compensate for the ¼ Hz frequency at which the data were collected. Accordingly, we multiplied the calculated data in Figures 3.11 and 3.12 by 2.3 to compensate for the ¼ Hz frequency at which the data were collected.

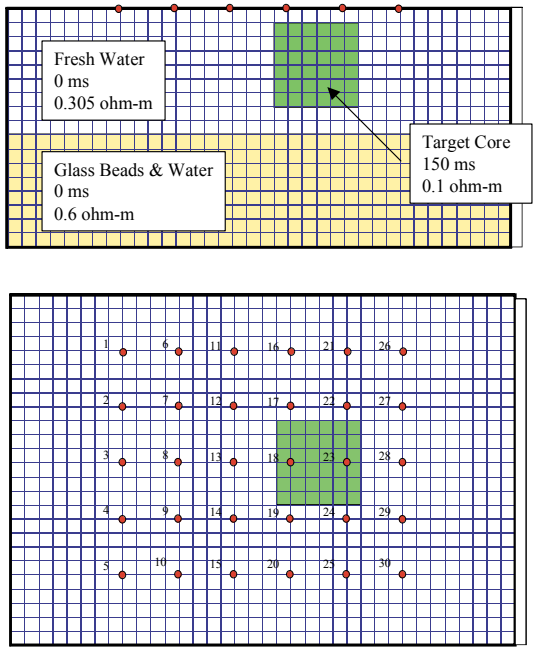

Rx Electrode 1	Rx Electrode 2	Vp Numerical Model (mV)	Vp Scale Model (mV)	IP Numerical Model (ms)	IP Scale Model (ms)
6	1	0.33	0.35	0.35	2.10
7	2	0.34	0.37	-2.29	-0.90
8	3	0.34	0.38	-3.65	-2.90
9	4	0.34	0.38	-2.24	-0.70
10	5	0.33	0.36	0.58	3.60
11	6	0.32	0.34	3.44	8.40
12	7	0.34	0.36	-3.32	4.80
13	8	0.35	0.36	-6.57	-0.40
14	9	0.34	0.36	-3.56	2.10
15	10	0.32	0.35	3.24	8.60
16	11	0.30	0.33	14.30	17.10
17	12	0.29	0.33	16.50	23.90
18	13	0.29	0.33	18.60	30.30
19	14	0.29	0.33	15.90	28.40
20	15	0.30	0.34	13.50	22.40
21	16	0.28	0.31	24.50	19.90
22	17	0.24	0.31	53.70	34.30
23	18	0.22	0.30	70.90	55.00
24	19	0.24	0.30	53.30	47.40
25	20	0.28	0.32	23.40	29.00
26	21	0.30	0.31	14.30	14.10
27	22	0.30	0.32	16.20	13.40
28	23	0.29	0.32	18.30	10.80
29	24	0.29	0.32	16.30	14.10
30	25	0.30	0.31	14.00	16.10

Figure 3.12: Numerical model calibration to 3" steel ball model immersed in an aqueous solution of 30,000 ppm NaCl (homogeneous target case).

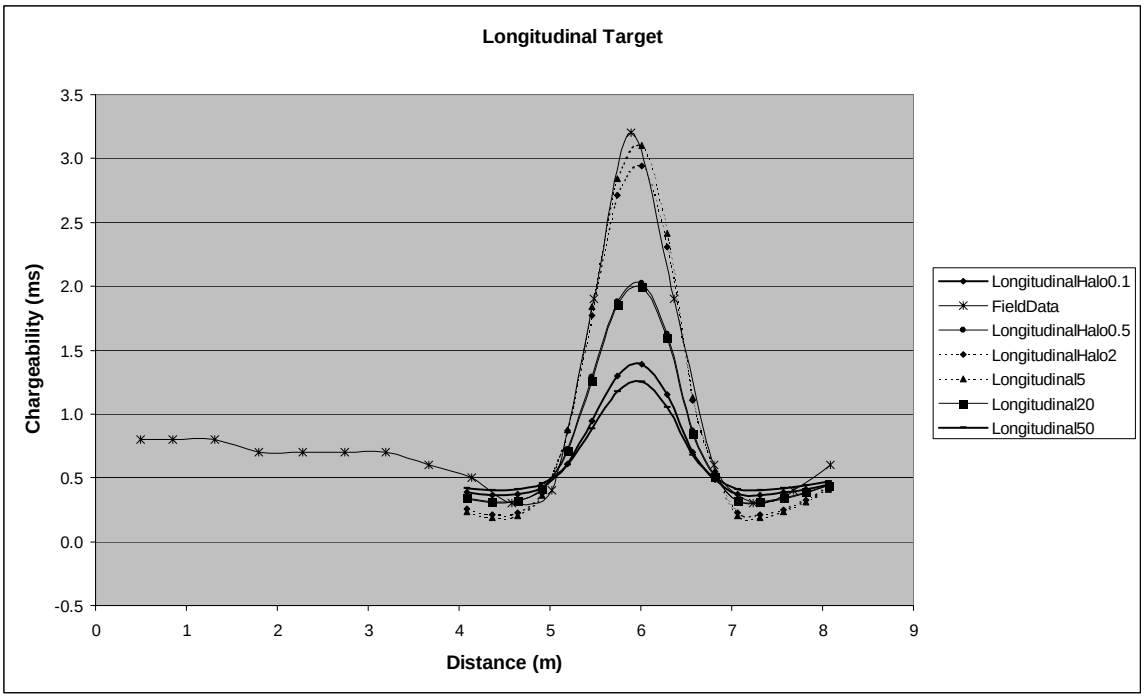

Figure 3.13: Calibration of model results to the longitudinal target field response by varying the resistivity of the resistive shell.

Ultimately, we collected field data at Mare Island at 8 Hz (section 5). The strongest IP response occurred over a five inch projectile (RA207) oriented longitudinally with respect to the array. Our models indicate that the transverse response is much weaker than the longitudinal response (Figures 3.13 and 3.14). In order to model the received amplitudes it was necessary to generate a new calibration employing the resistive shell model. We chose a very high intrinsic chargeability of 1000 mV/V, put the conductive core at 0.001 ohm-m resistivity and discretized the body using a 1 cm mesh. The resistivity of the 1 cm outer shell was varied from 0.1 ohm-m to 500 ohm. A peak in IP response occurs when the shell resistivity is 2-5 ohm-m. This numerical model accurately duplicates the observed result that the transverse response (Figure 3.14) is much lower amplitude than the longitudinal response (Figure 3.13).

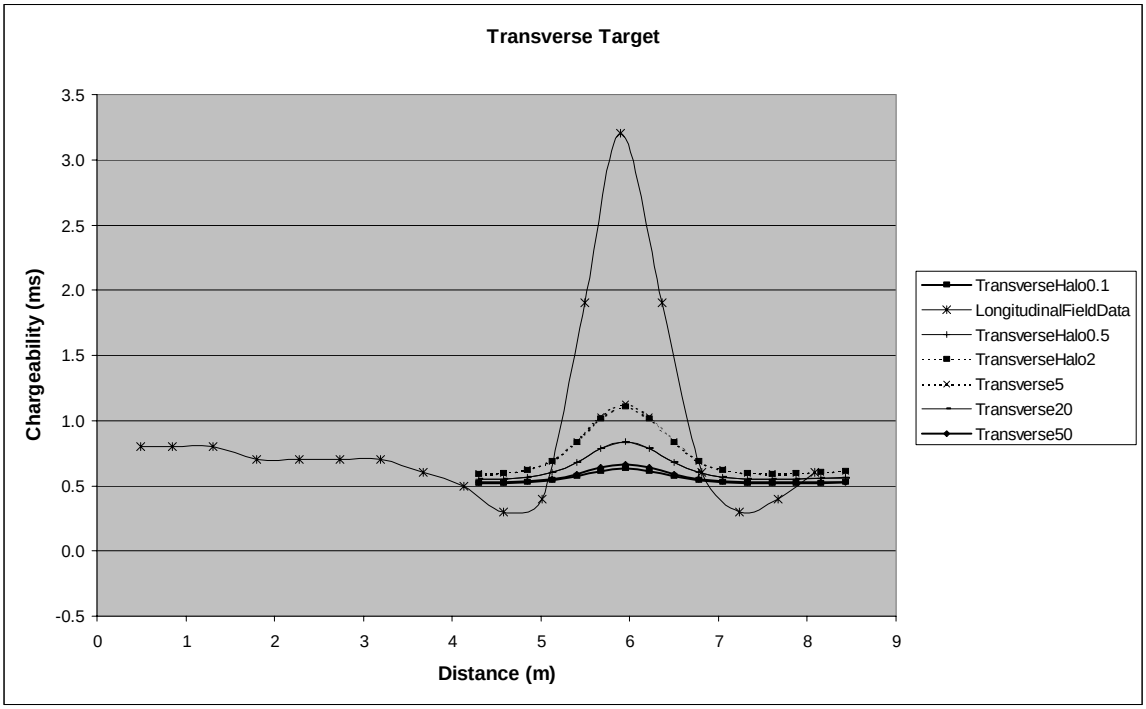

Figure 3.14: Comparative transverse responses for the model shown in Figure 3.13.

3.2.3. Sensitivity Study (Dipole Size and Target Detectability)

We used a deep-water (5 m) model and a small target (8" diameter by 24" length shell) for a preliminary study of model sensitivity. We used target parameters consistent with a fresh-water background.[9] After processing several standard arrays, we concluded that the target remained virtually undetectable. Subsequently, we chose the gradient array for a more comprehensive study of target detectability to the parameters of dipole size and target range. Three significant results were generated:

1. When the receiver dipole size is greater than 3/2 the largest dimension of the target, the target is virtually undetectable (Figure 3.15).

[9] Our laboratory experiments indicate that IP amplitudes are as much as 5 times larger when measuring these targets in a salt water host.

2. The maximum detection distance for a small target (relative to the dipole sizelength), for most standard arrays, is on the order of 4 dipole lengths (Figure 3.16).
3. For the simulation of the 8" projectile, the maximum dipole size length that produced a field-measurable signal was 1 meter. This dipole size length was employed for all subsequent modeling.

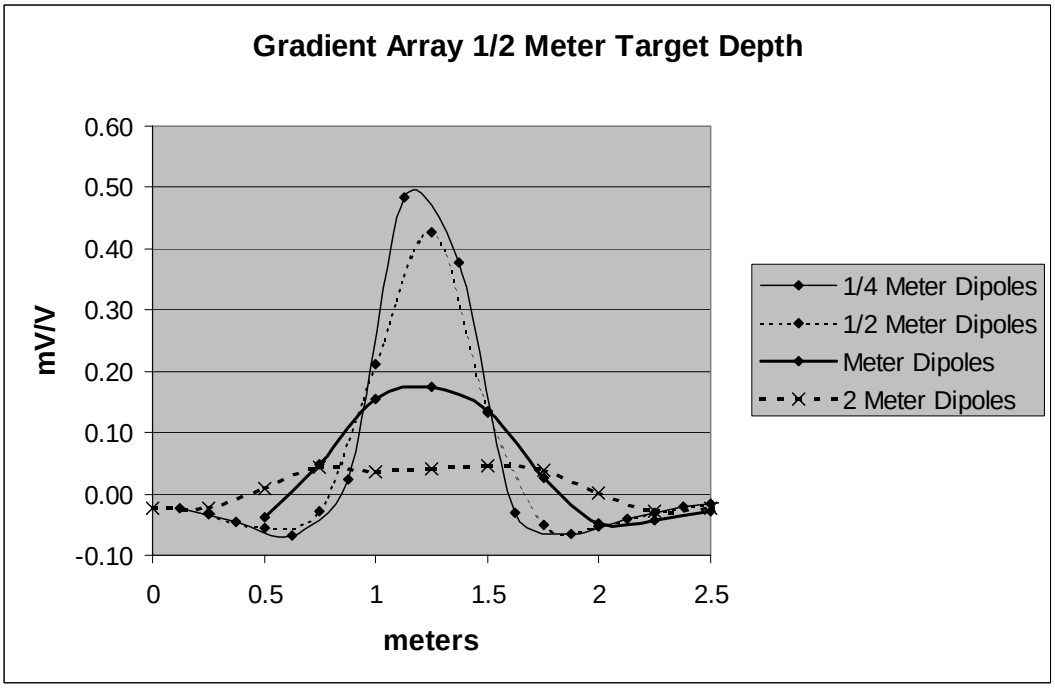

Figure 3.15: Dipole size comparisons for 5 m AB (1/4 and ½ m MN) and 10 m AB (1 meter MN) gradient arrays in fresh water.

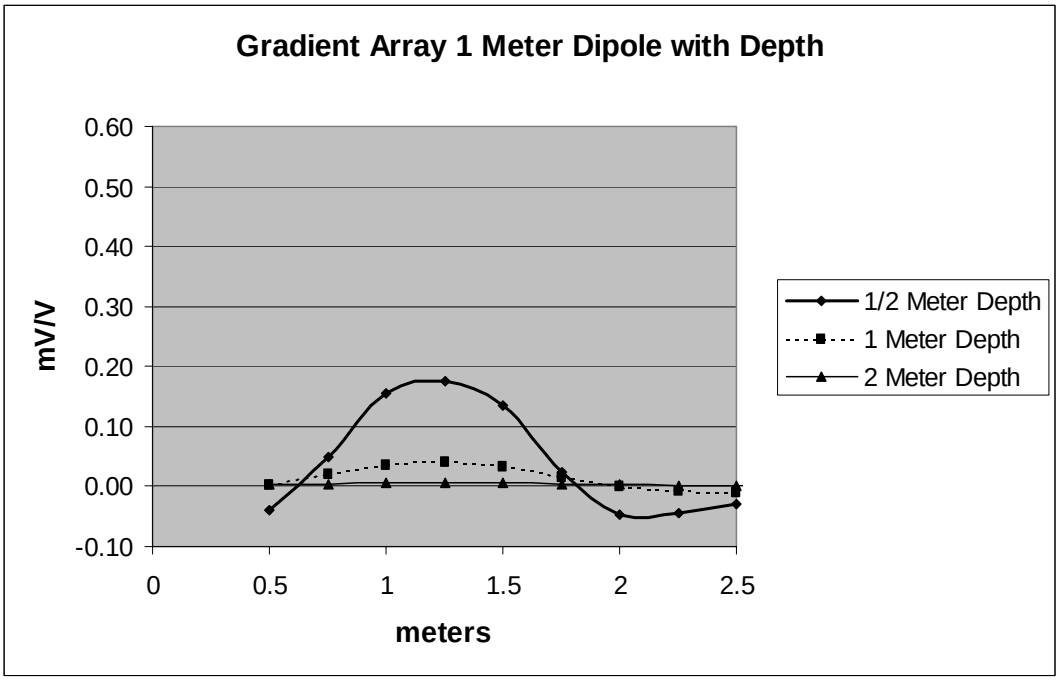

Figure 3.16: Target range for 10 m AB, 1 m MN Gradient Array in deep water

3.2.4. IP Array Comparisons

We scaled our calibrated models to an 8" by 20" (25 cm by 50 cm) target. Unless otherwise noted, we used a 1-m dipole for both transmitting and receiving. We tested several electrode geometries including the gradient array with several different "AB" separations; the Pole-Pole array; and the dipole-dipole (DPDP), Pole-Dipole, Ladder, and Vertical dipole arrays each with several different 'n' values and separations. The geometry for these electrode arrays is illustrated in Figure 3.18.

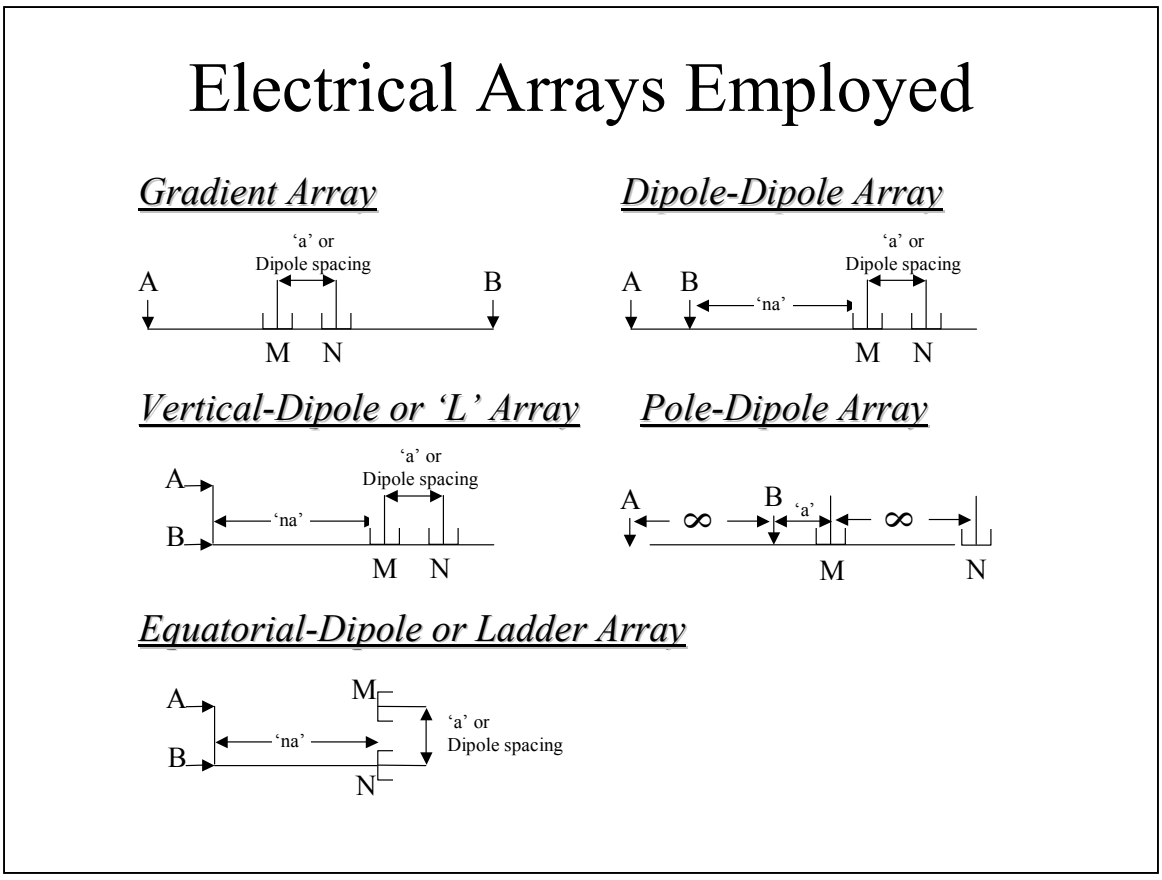

Figure 3.17: Array geometries employed during numerical model study.

In Figure 3.18 we compare peak IP response to target distance from the array in both fresh and salt water. An indication of the primary field strength, which can significantly affect the ability to measure field responses, is missing in Figure 3.18. When determining optimal arrays, it is necessary therefore to consider both primary signal strength and maximum IP response. In some cases (DPDP, Vertical DP and Ladder for large 'n'), primary signal strength may be a more significant factor than optimal IP response. Figure 3.18 alone, for example, would imply that the Ladder array is optimal. However, the plot does not indicate the magnitude of the received voltages and therefore we have no idea whether the signals are measurable.

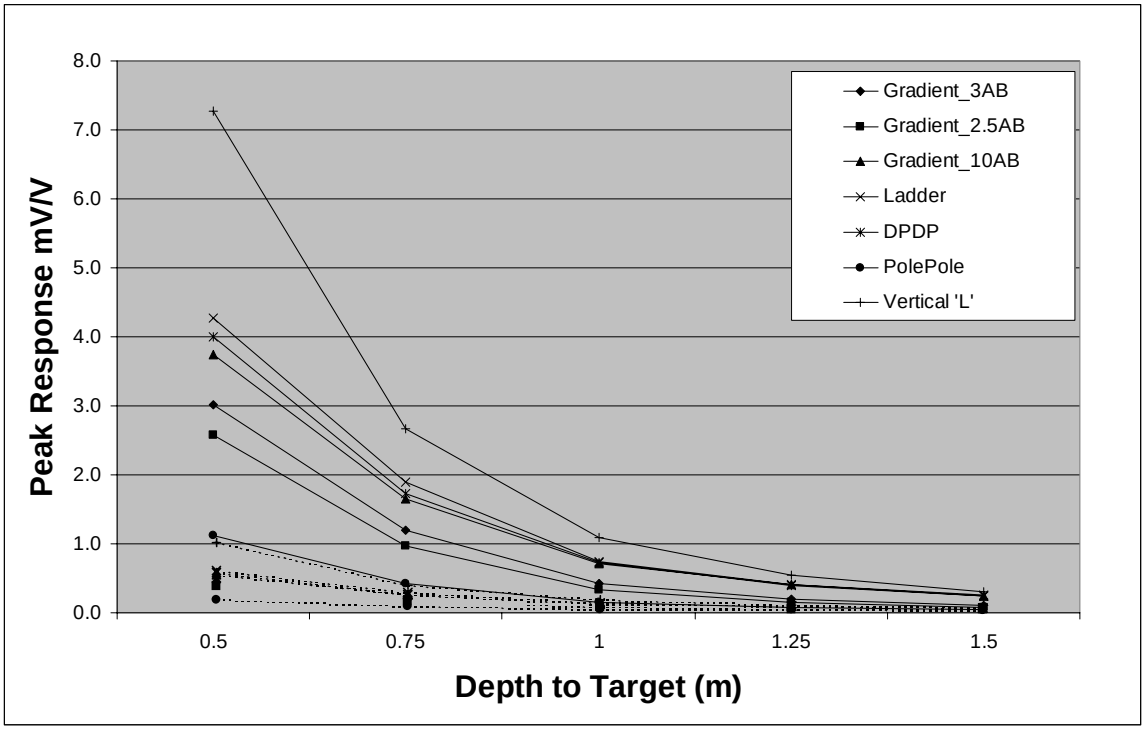

Figure 3.18: Peak IP response as a function of target depth for different electrode arrays. Curves with solid lines represent a salt water host while the dashed curves are results for fresh water.

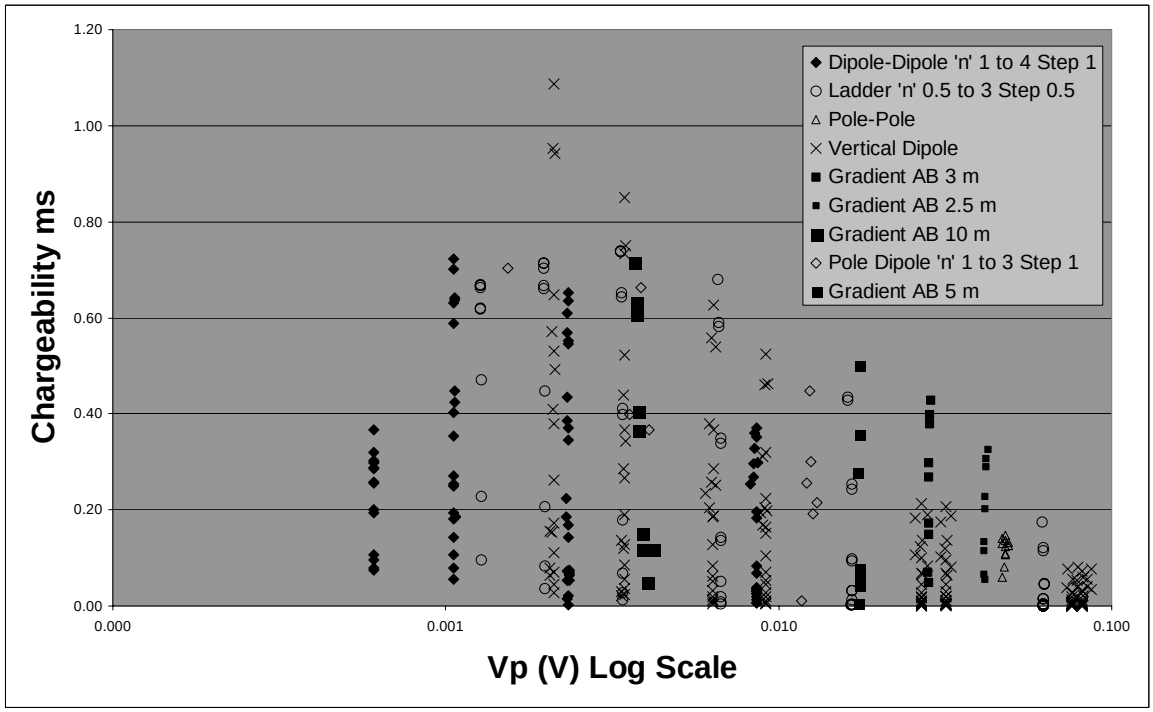

Figure 3.19: Comparison of IP response and primary voltage (Vp) for various array geometries.

In Figure 3.19 we have plotted IP response (chargeability) against primary (on-time) electrical potential (Vp). The plot includes results for several points along a profile 1 m above the target for several types of arrays and at several different "n-spacings" for each array. For each array, the data along the profile plots along a single, nearly vertical line, like a string of beads. The "strings" are nearly vertical since the change in the primary potential is very small for most arrays. The purpose of the "bead plot" is to provide a graphical means of comparing the responses of various arrays. The topmost point of each string shows the maximum IP response. Any curvature of the string shows the (generally small) primary response to the target. The optimal arrays are those that have both a large primary/signal response (ie. the string plots on the right side of the figure) and a large peak IP response.

Generally speaking, the selection of an optimal array will require a-priori knowledge of the measurement system noise under realistic field conditions. However, in many cases, one array has obvious advantages over another. For example, consider the pole-pole array results shown as yellow triangles in Figure 3.19 versus the 2.5 AB gradient array shown as maroon circles on the figure. From the position of the strings, we can see that the two arrays have almost the same primary amplitude, about 80 millivolts per amp. However, the peak IP response of the gradient array is almost 3 times as large as the peak response of the pole-pole array. Clearly, for the given target and configuration, the gradient array provides superior target resolution. Similarly, we can see that the DPDP array tends to have lower peak IP responses than other arrays with comparable primary potential magnitudes.

The gradient array and ladder arrays appear to be very comparable in target resolution. The vertical dipole array produces the largest chargeability response but only when the primary potential is small, less than 2 mV/A. For smaller "n-spacings" it produces much smaller

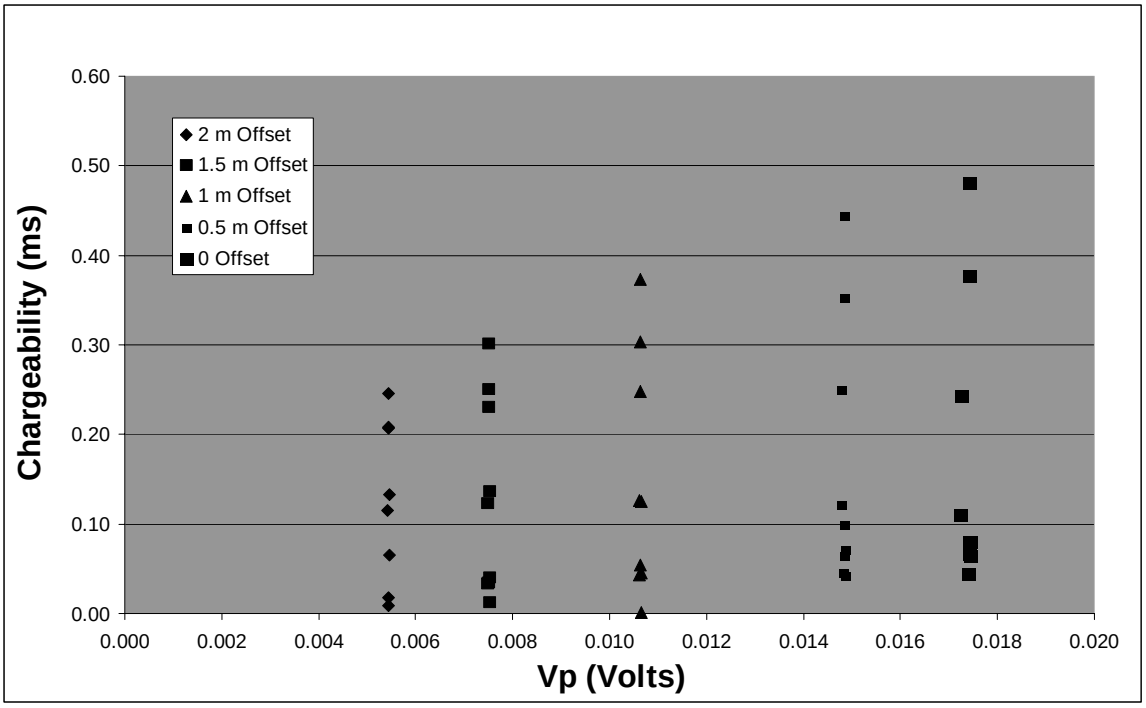

Figure 3.20: IP response versus primary field voltage for a 5m AB offset gradient array. The parameter is the lateral offset of the receiver dipole from AB.

chargeabilities than gradient and ladder arrays (Figure 3.19). The offset-gradient array is a hybrid of the gradient and ladder arrays. The array uses a relatively long source dipole like the gradient array with a series of short receiver dipoles offset to the side of the transmitter. The goal of this array is to retain the optimal response of the gradient array while acquiring data over a wider region. Figure 3.20 shows the bead plots for an offset gradient array with an AB of 5 m and receiver offsets of 0 to 2 m. While Vp drops by a factor of 3 in 2 meters, the IP response has decreased less than 50%. From Figure 3.20, it appears that a lateral sweep of up to 1.5 meters should be possible with a gradient array of 5 m AB. This configuration was deployed in the field. We saw a slightly greater drop in IP (60%) and lesser drop in Vp (30%) which is explained by a modified configuration that deployed the receiver electrodes at a deeper level than the transmitter.

3.3 Preliminary Study Conclusions

This preliminary study has demonstrated that a measurable IP response is associated with metallic objects in equilibrium with an (aqueous) electrolyte. The response is significantly greater when the electrolyte is salt water. Furthermore, when the object is small it may be presumed to behave as a point dipole. Our laboratory experiments were performed on a spherically shaped object placed in a relatively uniform polarizing field. The resulting observations were fit well using a point dipole oriented in the direction of the applied electric field (i.e., horizontal).

Using calibrations based on laboratory measurements, the numerical modeling allowed us to expand the physical scale of our study to estimate performance at useful field scales. Our numerical models suggest that Marine detection of UXO using the IP method is indeed feasible. The modeling study produced the following results:

- The receiver dipole size should be no more than double the long dimension of the target, and the depth to target should be no more than 1 dipole sizelength.
- The short AB gradient and ladder arrays provide the best combination of signal strength and IP response.
- Target orientation is significant; the strongest response occurs when the longest dimension of the body is oriented parallel to the primary field (generally horizontal).
- EM coupling (not shown but studied during the project) is insignificant because the array size deployed is small (5 meters) and relatively low frequencies are used (8 Hz in the field).

4. Assembly of Full-Scale System

Our preliminary study suggested that full-scale experiments should be carried out with a gradient array with an AB (Tx dipole length) on the order of 5-10m. Those studies also demonstrated that the lateral range of detection might also be expanded if the receiver array consisted of receiver dipoles that were laterally offset from the AB axis. Our objective in assembling a full-scale system was to confirm our preliminary studies by detecting and mapping the IP response from buried metallic objects in very shallow water. Therefore, we elected to assemble an electrode array that was to be deployed on the water surface.[10] Figure 4.01 is a block diagram showing the elements of the system. We will briefly discuss each of the system elements in the remainder of this section.

The major subsystems of the equipment are:

- Resistivity Measurement Subsystem
- Electrode Array
- Data Acquisition Subsystem
- Navigation Subsystem

4.1 Resistivity Measurement Subsystem

The resistivity measurement subsystem is based on standard Zonge equipment. The receiver is an 8-channel GDP-32^{II} capable of time domain or frequency domain measurements. The acquisition program (TDIP) was modified to permit continuous acquisition at a selected base frequency and stacking constant. Regrettably, limitations in the TDIP software related to data storage and display limited the maximum report rate to approximately 1.15 samples/sec irrespective of frequency or stack count. This limitation in the maximum report rate can easily be overcome.[11] It was beyond the scope of this project, however, to make the software modifications necessary to significantly improve the report rate. The receiver has a real time clock with sub-second precision (~4ms) that can be electronically synchronized with UTC time. Each data frame is time-stamped with its acquisition time to facilitate merging the data with GPS position data. The transmitter is battery-operated and requires a 24-V dc supply. The transmitter will supply 4-6A current. At these current levels, the signal level of the primary voltage at the receiver electrodes (i.e., the voltage while the current is on) is on the order of 40-50mV, more than sufficient for a good IP measurement.

[10] At the time we designed our electrode array, it appeared that it would be necessary for us to construct our own test bed, presumably in a tidal zone or very shallow fresh water.

[11] Based on the performance of the GDP-32^{II} in dynamic TEM data acquisition, we believe report rates of up to 32 or even 64 samples/sec are obtainable. But such sample rates require major changes to the storage and display routines of the Zonge receiver.

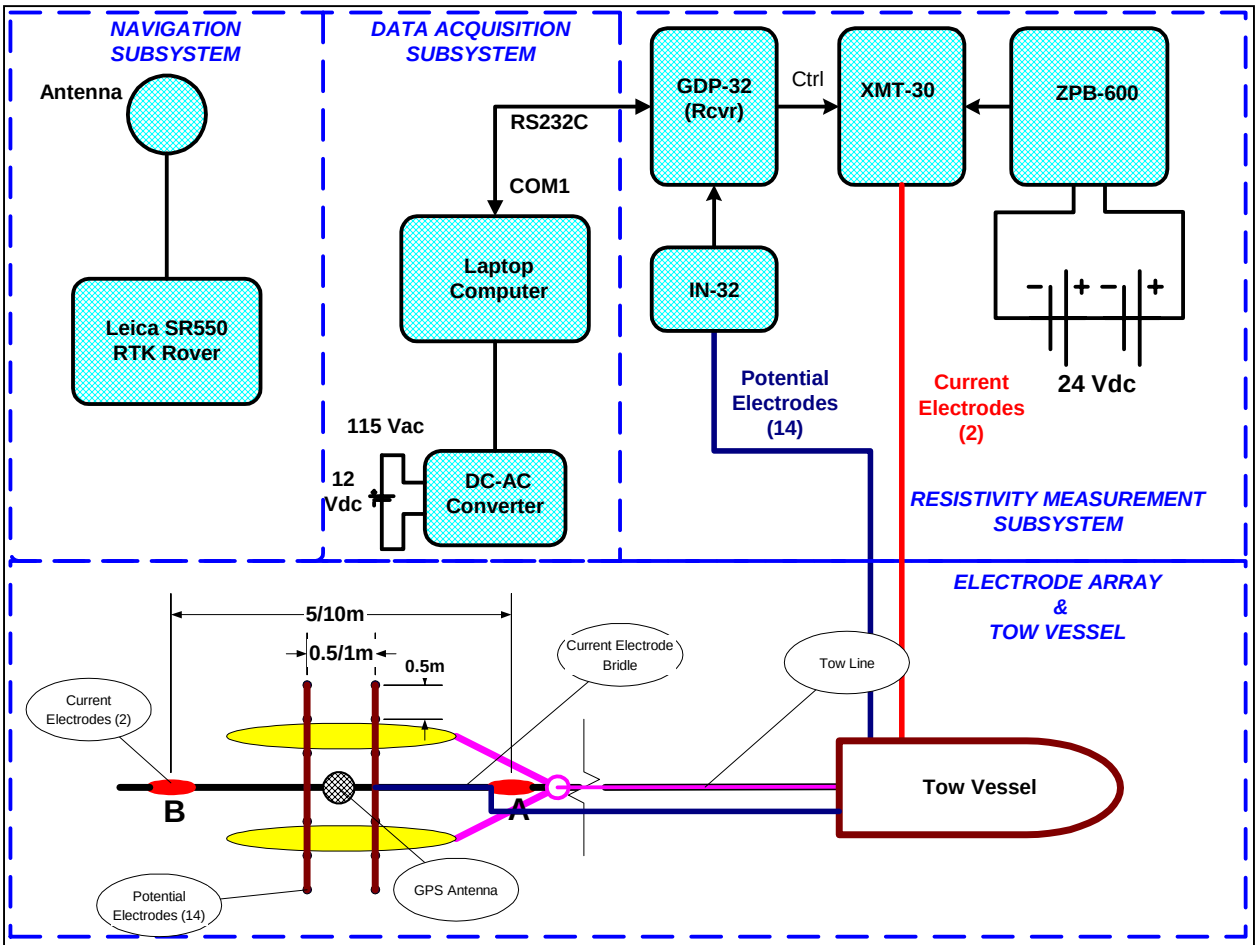

Figure 4.01: Block diagram showing major functional elements of the system assembled for full-scale field

4.2 Electrode Array

In accordance with results from our preliminary study (Section 2), we designed and assembled an offset gradient electrode array consisting of 2 current electrodes (A & B in Figure 3.02) plus 14 receiver electrodes. The receiver electrodes are organized as 7 dipoles distributed laterally across the center of the current electrode pair. We have annotated the photograph in Figure 4.02 to show the current and potential electrodes. Note that the Ag-AgCl receiver electrodes are mounted on PVC rods (1/2" pipe). This allows the receivers to be deployed as much as ½ m below the water surface. As we noted in the previous section, the gradient array provides good IP response together with reasonably high primary fields (Vp) and is easy to deploy. The 7 receiver dipoles are spaced laterally either at ½-m or ¼-m intervals.[12] The 15th receiver electrode at the center of the current dipole was used as a reference electrode. The electrode array covers a 3-m wide swath during surveys. The receiver dipole spacing is adjustable from ¼-m to 1-m. For larger targets, the 1-m receiver dipole provides a larger signal. For smaller targets, receiver dipoles that are very much larger than either a characteristic target dimension or a target depth will result in a complex multi-peaked anomaly shape. Therefore, when we deploy the system with the larger current dipole (i.e., AB = 10m) and correspondingly larger receiver

[12] The lateral spacing is adjustable to ¼ m. However, we did not use the ¼-m spacing in any of our tests.

dipole (i.e., MN = 1m), we will be optimized to detect the larger and probably deeper targets.

4.3 Data Acquisition Subsystem

The GDP-32^{II} receiver records data automatically, therefore the data acquisition system is redundant. Each data record is stored in a data file on mass storage device (compact flash memory) of the GDP-32^{II}. In its present (uncompressed) format, the receiver is able to store many hours of data (~4,140 records/hr). With the implementation of binary storage, the standard 256MB compact flash card can easily store several hours worth of data even with sampling as high as 16 or 32 samples/sec. Although the GDP-32^{II} receiver is capable of reporting a subset of the data from each record via its RS-232 serial (COM) port in real time, that capability was not used during our field experimentation.

Figure 4.02: Annotated photograph of electrode array used in full-scale experiments.

4.4 Navigation Subsystem

The instantaneous position of the receiver electrode array is determined by a Trimble Pathfinder Asset Surveyor that provides satellite corrected differential GPS positions (DGPS). This system provides "Subsub-meter" level accuracy positions (horizontal coordinates) at a rate of 1 Hz.[13] The GPS data are merged with the time-stamped IP data during a post-processing step, after determination of a latency correction to account for time offsets between the GDP and GPS system clocks (this is discussed further in sections 5.3.4 and 5.3.5).

4.5 System Deployment

As Figure 4.01 suggests, the normal mode of deployment will be to tow the electrode array behind a small vessel. In this deployment mode, the operator and equipment are in the vessel. Because of our slow sampling speed, we tow the array at the minimum speed necessary to maintain steerage (~2 kts or 1 m/s)[14] of the 5 m array. At very low water levels, we attempted to acquire some static data using Zonge's complex resistivity acquisition program (CR) by making fast each end of the transmitter bridal cable as if they were bow and stern docking lines.

The system that we have described has excellent flexibility because it is easy to change the spacing of both the receiver and transmitter electrodes. Its main limitation is that it must be deployed from the surface, therefore water depth is a factor affecting the ability to detect targets. Further development of the IP method for UXO detection will require an electrode "sled" that can be dragged along the bottom or "flown" close to the bottom in order to maximize the probability of detecting small targets on the bottom and larger targets that may be a meter or more below the bottom.

---

[13] We originally planned to use a Leica SR530 RTK GPS system that provided centimeter-level accuracy in positions. Unfortunately that system was unavailable during the time of our field experiment at Mare Island.

[14] The Mare Island site was subject to very strong tidal currents. Moving against the current, we often achieved bottom speeds of less than 1 knot. But, of course going the other way bottom speeds were higher.

5. Experiment at the Mare Island Naval Shipyard

We conducted our field experiments at the Mare Island Naval Shipyard (MINS). Located at the north end of San Francisco Bay, MINS was used primarily for ship building and repair from 1854 until it was closed in 1996. From 1857 to 1975, MINS was a site involved in the manufacture, storage, and transfer of naval ordnance [24]. As part of a program to evaluate ordnance detection equipment and technologies, the U.S. Navy constructed both a Reference Area and a Test Area on a shallow water site within the littoral tidal range on the southeastern shore of Mare Island. The reader may consult the VDS final report produced by Environmental Chemical Corporation (ECC) under contract to the Navy for details of the construction of these sites [24]. We have extracted from that report graphics showing the location of the aforementioned sites.

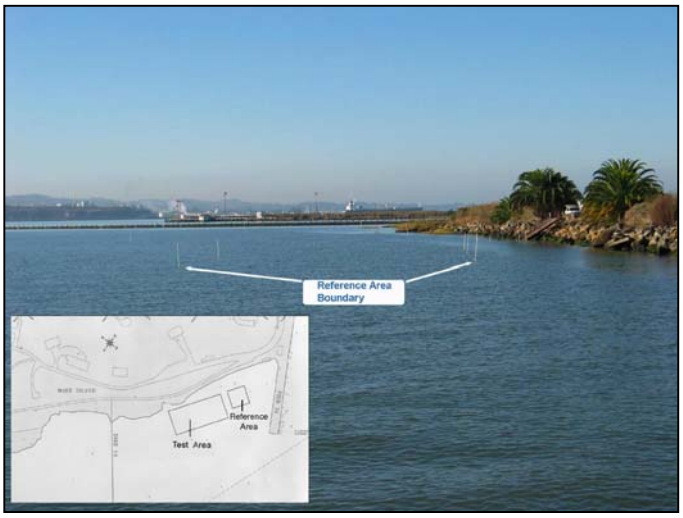

Figure 5.01: Photograph and location map (inset) of VDS test areas at Mare Island.

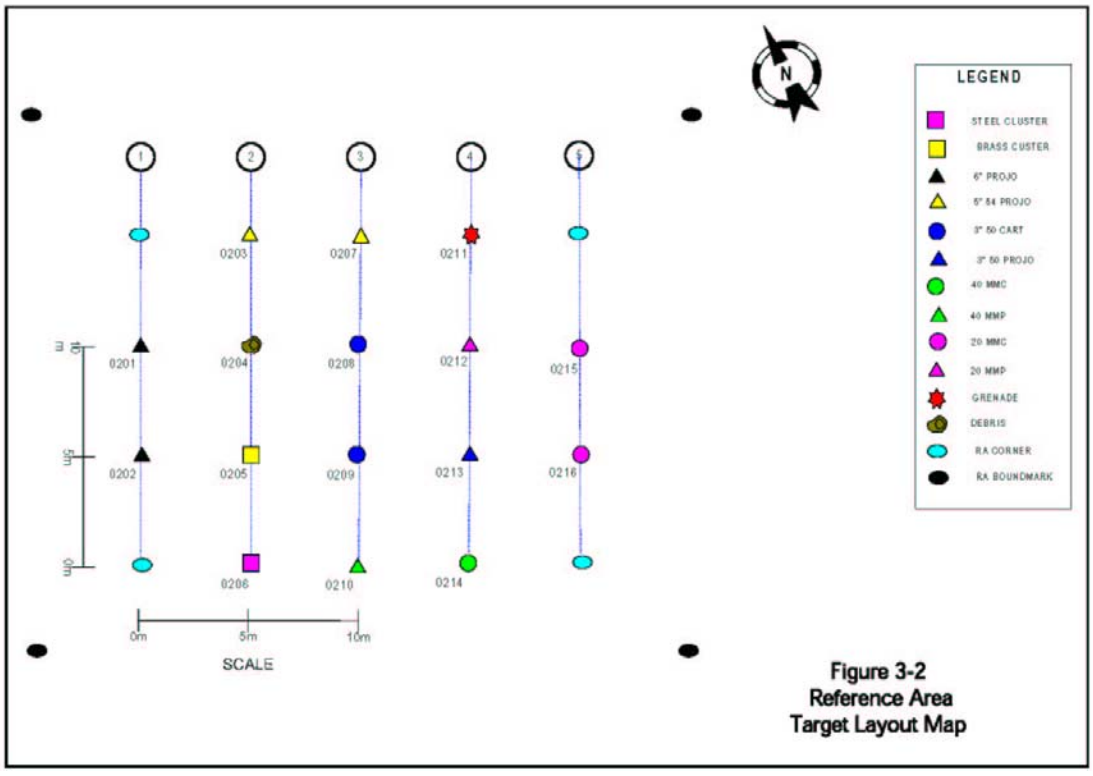

Figure 5.02: Reference area target map. (Figure 3-2 in [20])

5.1 The MINS Reference Area

We conducted our tests over the Reference Area, a 20 m by 15 m rectangular area seeded with 16 targets. Figure 5.01 shows the location of the Reference Area relative to pier 34 and dike 14. Both sites are within the tidal range, and at extreme low tides, they are above sea-level. The Reference Area was of particular interest to us because the target identity, location, and orientation have been provided by ECC in their final report. Figure 5.02 shows a detailed plan view of the Reference Area. The targets are identified by the shape and color of the symbols as indicated in the legend. John Bowles, the ECC Project Manager for MINS, provided us with GPS locations for the targets in the reference area. We have tabulated those locations as Table 5.1 since they are not available in the VDS Test Program Final Report that is the source of all of our information regarding these sites [20].[15] Table 5.2 contains a description of the targets along with their subsea depth of burial.

Table 5.1: MINS Reference Area Target Locations

MINS Reference Area Coordinates (WGS84 - NAD83 - UTM Zone 10N - Meters)		
ID	**X**	**Y**
RA201	565904.86	4214507.82
RA202	565902.06	4214503.53
RA203	565911.23	4214509.43
RA204	565908.81	4214505.19
RA205	565906.46	4214500.97
RA206	565904.34	4214497.16
RA207	565915.83	4214507.08
RA208	565912.93	4214502.68
RA209	565910.71	4214498.29
RA210	565908.34	4214494.11
RA211	565920.06	4214504.74
RA212	565917.50	4214500.14
RA213	565915.18	4214495.61
RA214	565912.53	4214491.50
RA215	565921.78	4214497.64
RA216	565919.27	4214493.32

Table 5.2: Target Descriptions and Depth of Burial.

Target No.	Depth (meters)	Target Description
0201	01.20	6" SIMULATED PROJECTILE, FLAT, PARALLEL W/LINE
0202	00.61	6" SIMULATED PROJECTILE, FLAT, PERPENDICULAR TO LINE
0203	01.20	5"54 PROJECTILE, NOSE DOWN
0204	00.00	DEBRIS, COIL WIRE ROPE, FLAT
0205	00.00	CLUSTER, BRASS
0206	00.00	CLUSTER, STEEL
0207	00.61	5"54 PROJECTILE, FLAT, PARALLEL W/LINE, OGIVE S
0208	00.61	3"50 CARTRIDGE, FLAT, PARALLEL W/LINE, OGIVE N
0209	00.61	3"50 CARTRIDGE, FLAT, PERPENDICULAR TO LINE, OGIVE W
0210	00.30	40MM SIMULATED PROJECTILE, FLAT, PARALLEL TO LINE, OGIVE S
0211	00.00	GRENADE, FLAT
0212	00.61	20MM PROJECTILE, FLAT, PARALLEL W/LINE, OGIVE N
0213	00.61	3"50 PROJECTILE, FLAT, PARALLEL W/LINE, OGIVE S
0214	00.30	40MM CARTRIDGE, FLAT, PERPENDICULAR TO LINE, OGIVE E
0215	00.15	20MM CARTRIDGE, FLAT, PERPENDICULAR TO LINE, OGIVE E
0216	00.61	20MM CARTRIDGE, FLAT, PERPENDICULAR TO LINE, OGIVE W

[15] The position coordinates were sent to us several days after we started our experiments. It was not until after we had demobilized and started data reduction in earnest that we discovered that there were what appears to be systematic errors between the GPS positions that we recorded using the Trimble system and the position coordinates furnished us by ECC.

5.2 Mobilization and Logistics

The test plan was submitted to both SERDP and the Navy Facilities Command in mid September. The plan called for mobilization to the MINS site late the week of 12 October 2003. We commenced our experiments on Monday, 20 October. We completed those experiments on Friday, 24 October. Logistics and other arrangements were provided to Zonge and MPT personnel by EG Engineering (Sausalito, CA). EG Engineering provided a shallow water outboard motor-powered boat that served as the tow vessel for our electrode array. The photographs in Figure 5.03 show details of the installation. We completed the installation of the equipment in about 5 hours on 20 Oct. We spent the rest of the day in shake-down tests. These tests revealed minor problems with the acquisition software that were not discovered during bench tests in Tucson. These problems required that the code be modified and reinstalled. The necessary modifications were carried out in Tucson and e-mailed to us so that we were operational the following day.

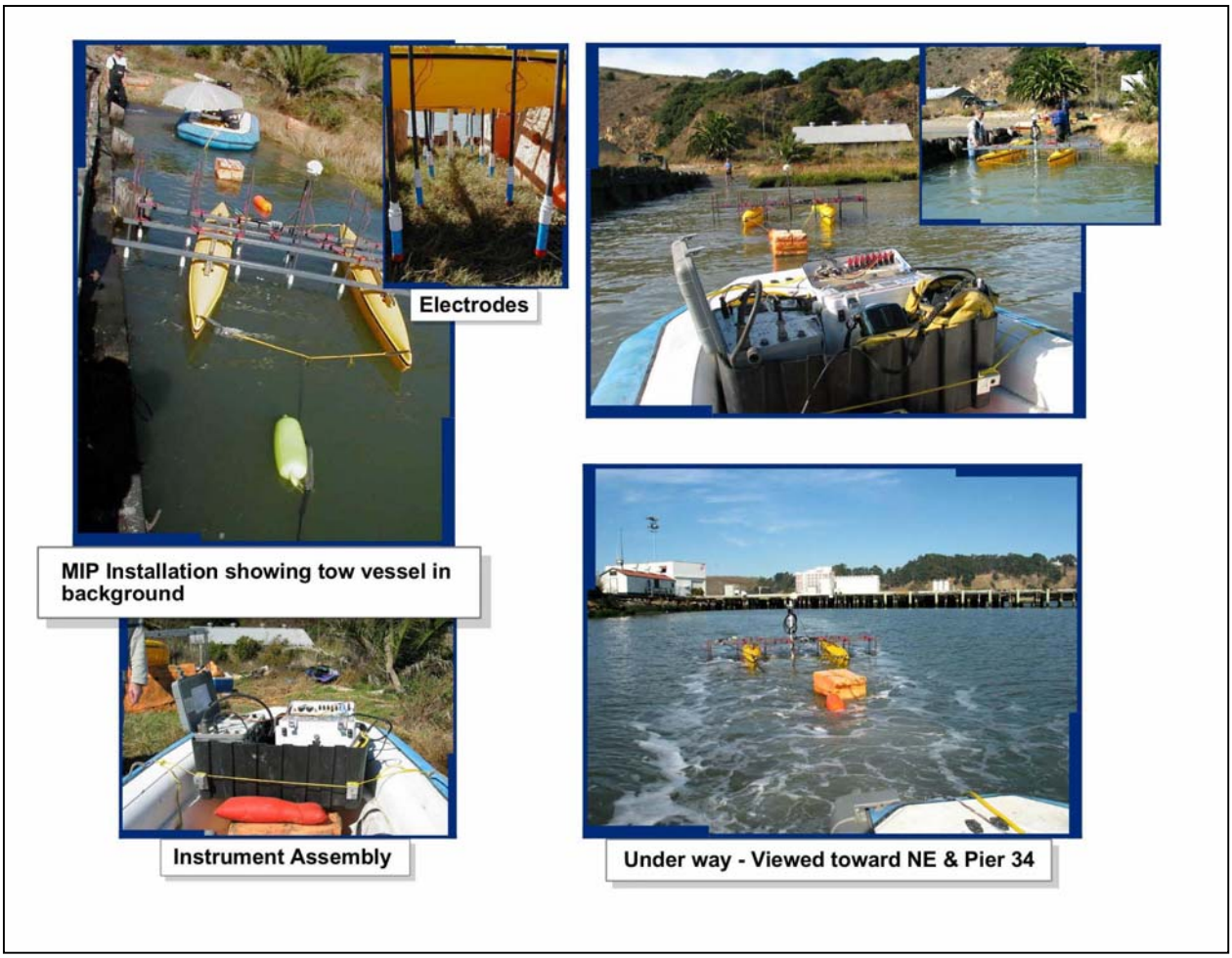

Figure 5.03: Photographs showing details of equipment used during full-scale tests at MINS.

Table 5.3: List of activities and array configurations according to demonstration data.

Date	Activity	AB (m)	MN(m)
18-Oct-03	Mobilization	na	na
19-Oct-03	Mobilization	na	na
20-Oct-03	Setup & Preliminary Tests	5	0.5
21-Oct-03	TDIP	5	0.5
22-Oct-03	TDIP/CR/Latency	5	0.5
23-Oct-03	Data Reduction & Eval	na	na
24-Oct-03	TDIP	10	1
25-Oct-03	Demobilization	na	na
26-Oct-03	Demobilization	na	na
27-Oct-03	Demobilization	na	na

5.3 Experiments

Our plan called for us to conduct repeated surveys over the Reference Area using two array geometries: 1) AB = 5m, MN = ½ m; and 2) AB=10m; MN = 1m. Because of the tidal range (~2 m) at Mare Island, we were only able to survey at or near low tide. During our field experiments, low tides were occurring very early in the morning (4:30-7 am) and very late in the afternoon. At high tide, (generally around local noon time), the water was too deep over the Reference Site (well over 2 m) for us to have any chance of detecting targets. We monitored tidal height during our surveys by observing the water-level on a graduated section of PVC pipe (1-ft graduations) located adjacent to the Reference Area. We compared a reading from the graduated pole with a measurement of water depth in the center of the Reference Area to determine a correction (+0.4m) between the water depth at the graduated pole and the average depth in our survey area.

For the most part, survey traverses were directed NE-SW because in those directions, we had ample room to run beyond the area boundaries and maneuver during turn-around. We did attempt to acquire some data in the transverse direction (NW-SE). There is very little room, however, to maneuver between the NW boundary of the Reference Area and the shore when surveying in that direction. Survey tracks are not included on the maps in order to reduce visual clutter. Survey tracks are in the NE-SW direction unless explicitly stated otherwise.

5.3.1. Measurement Electrode Depth

We conducted some preliminary tests over the Reference Area to test our acquisition software and to measure overall background noise levels. These early tests were conducted with the measuring electrodes set for a depth just sufficient that they were totally immersed in the water (~5cm to electrode center). After we determined that we were unable to measure an IP response at moderate water depths over the Reference Area (~1.2m, ~3.8 ft), we adjusted the electrode depth to their maximum depth (55cm ≈ 27 in) in order to minimize the distance between the electrodes and the bottom. Unless otherwise noted, all measurements were taken with the measuring electrodes set at a depth of 55cm.

5.3.2. Time Domain IP Measurements

We had originally planned to acquire multi-gate time domain data (13 gates linear-spaced in

time) for these experiments. However, during our initial trials, we determined that our maximum report rate while in this mode was in excess of 2 sec. We subsequently disabled the multi-gate function in a version of the TDIP acquisition program and were able to achieve a report rate of 1.15 samples/sec – still not good, but significantly better than ½ sample/sec when acquiring the full transient on 8-channels. The slow report rate is principally a function of the number of active channels (8 for this experiment), the amount of post acquisition processing (principally the windowing of transients into 13 windows or gates), and perhaps most importantly updating the receiver display and storing the data. The simple expedient of eliminating the calculation of all but the chargeability window (equation 15) eliminates much of the calculation, display, and storage overhead time. Even so, it still requires about ½ sec to complete these tasks before the receiver can commence acquiring a new data sample. With some optimization (e.g., elimination or minimization of display updates, and binary data storage), the required overhead time can be reduced to less than 33 ms (as we have shown in the case of dynamic TEM data acquisition). The time domain data that we show here has been acquired at a base frequency of 8Hz with a stacking constant of 2 (i.e., 2 cycles per sample). The effective sample rate for these data was 1.15 samples/sec.

5.3.3. Complex Resistivity Measurements

We acquired a small amount of broadband complex resistivity data (CR) using Zonge's standard CR measurement sequence. These data cover a frequency range of $0.125 \leq f \leq 72$ Hz. To cover this range, we transmit a nominal bipolar 100% duty-cycle square wave at 3 different base frequencies, 0.125Hz, 1.0 Hz, and 8.0 Hz, respectively. The received signals, including a channel that measures the current waveform, are analyzed for the first 5 odd harmonics (1^{st}, 3^{rd}, 5^{th}, 7^{th}, and 9^{th}) for each of the fundamental frequencies to provide samples of the complex resistivity (amplitude and phase) at 15 frequencies.

We used CR measurements of the background (i.e., in relatively deep water where effects from the bottom and, possibly, from UXO would be small) to confirm our conclusion from the preliminary study that electromagnetic coupling effects for our array are small and can be ignored, particularly when measurements are made in the time domain. We also gathered a CR spectra with our electrode array stationed over the most prominent target in the Reference Area (RA207). The objective of the CR measurements over the target was to see whether there were any distinguishing features of the CR spectra associated with the target.

5.3.4. Latency Experiments

Our navigation data and IP data were acquired separately. Each datum is time-stamped with the GPS time. However, for various reasons, there is invariably a time delay between the times recorded by the GPS survey system (in this case the Trimble Pathfinder) and the time held in the GDP-32^{II} receiver. Most of the time difference is caused by the fact that time in the GPS data recorder are recorded as GPS seconds while the real time clock in the GDP-32^{II} is electronically set to UTC. Subsequent reduction by Trimble and other software simply converts times to date plus hours, minutes, and seconds without compensating for leap seconds. A correction of 13 seconds must be applied to account for leap seconds (GPS time is ahead of UTC time by 13 seconds). There are also small time latencies that occur between the GPS and GDP systems. For example, there is a small time latency introduced between the GPS second boundary and the corresponding second boundary in the GDP introduced by software latency. Also, there is a time

latency between the time stamp applied to the GDP data and the effective center of the data sample. This latency is largely a function of when the clock is read during the data cycle (usually at the end). In any case, there invariably exists a constant time latency or difference between the GPS clock and the GDP clock that is best determined experimentally. We determined the latency corrections for our data from Mare Island experimentally by repeated traverses in opposite directions over a fixed target. In the next section, we will show results from latency experiments over two different targets.

5.3.5. A Word About Target Positions

In Table 5.1, we have tabulated the UTM coordinates for the positions of the 16 targets in the Reference Area. When we overlaid these target positions with our maps, we found that there were significant offsets between target anomalies and target positions. Furthermore, these offsets are not necessarily constant from survey to survey. Although our Pathfinder GPS positions were all corrected to provide nominal "sub-meter" accuracy, we believe that the offsets we observe between the coordinates supplied by ECC and the positions of our targets is the result of two effects:

1. A constant offset in the either the coordinates of the survey control points located on Pier 34 that was used by ECC or, perhaps more likely, a small error in the position ephemeris for the satellite supplying the differential corrections.
2. Long-period, time-varying errors in the satellite differential corrections.

Unfortunately, we did not realize that we had a problem with our positions (relative to the ECC positions) until after we had demobilized. Otherwise, we would have located the 3 survey reference points with our system. In retrospect, we should have done that for no other reason than to provide a measure of reliability of our positioning system. In any case, we acquired many data sets over the Reference Area using different electrode array configurations and data acquisition programs. Target RA207, a 5-in 54 projectile (see Table 5.2) was the most prominent target in the Reference Area. We were able to map that target at most water depths and with both electrode array configurations. We picked the position of the peak IP response over the RA207 target for 8 of our good data sets acquired on 4 different days. The 8 positions, their corresponding means, and their standard deviations are shown in Table 5.4. Comparing the position for target RA207 as determined by ECC (Table 5.1) with the average position in Table 5.4, we found the offset to be 2.61m in Easting and 0.11m Northing. Accordingly, we have subtracted these offsets from the target coordinates in Table 5.1 and have used the resulting "corrected target positions" in the generation of maps showing the locations of the targets.

Table 5.4: UTM coordinates of RA207 target picks based on Trimble Pathfinder DGPS positions.

Source Data	Easting	Northing
CR Static - 22 Oct	565913.13	4214506.88
21Oct_Sprd6	565913.04	4214507.56
21Oct_Sprd7	565913.81	4214505.23
21Oct_Sprd8	565913.03	4214506.18
23Oct_Sprd6	565912.75	4214507.12
24Oct_Sprd3	565913.03	4214507.21
24Oct_Sprd4	565912.75	4214507.59
24Oct_Sprd5	565914.25	4214507.96
Average	**565913.22**	**4214506.97**
StdDev	**0.53**	**0.88**

5.4 Survey Results

5.4.1. Time Domain

AB= 5 m, MN= ½ m (Decay Plots)

As we indicate in Table 5.3, our first surveys were conducted with the electrode array configured for a 5m AB (Tx dipole) and a ½ m MN (Rx dipole). The transmitter dipole length controls the maximum practical depth of exploration.[16] Thus the 5m AB with the shorter (0.5m MN) receiver dipole is optimized to detect smaller targets at shallow depths. Figure 5.04 is a summary plot with a profile (a), a chargeability map (b), and some decay transients (c) on a profile crossing the peak of target RA207. Spreads 4 and 5 were the only data sets acquired over the Reference Area using the multi-gate version of our TDIP acquisition program. Consequently, the IP was sampled at a low sample rate (0.5 samples/sec). The water level was at 1.2 m and the receiver electrodes were 5cm deep. Note that the largest anomaly was 0.51ms (see color bar) and it occurred in close proximity to the plotted position of target RA207. Although the anomaly is clearly detectible on the profile (Figure 5.04a), it is not clear on the chargeability map (Figure 5.04b). During acquisition of this Spread, the targets were a minimum of nearly 1.2 m from the receiver electrodes and the anomalies are undersampled. However, Spreads 4 and 5 (Figure 5.05) are the only time domain data that were acquired using multi-gate TDIP. Figure 5.04c is a plot of IP transients for points along a profile crossing target RA207. Even at very low IP signal levels, the transient corresponding to the anomaly peak (magenta curve) is still prominent against the background. Note how the non-anomalous transient curves tightly together and the data points appear to have a granularity. In particular, when we view the chargeability curve with an expanded scale, we can see a distinct granularity of 0.1ms, suggesting to us that the noise level in these data is almost an order of magnitude (20dB) lower than we are accustomed to seeing in land data. As a result of these and other data, we modified our acquisition program so that we added another significant digit to the IP data we stored.[17]

[16] One often quoted rule of thumb for resistivity sounding is that more than half the transmitter current flows between the depths of 0 to AB/2. Transmitter current density (or more properly electric field) controls the strength of IP polarization. Therefore, applying this rule of thumb, one might say that it is unlikely that any target regardless of size would be detected at depths greater than AB/2 (2.5m in this case). Of course there are other important variables, such as target size, and resistivity contrast between the sea-water and the sub-bottom that are also important.

[17] The standard Zonge TDIP program stores chargeability (M) to the nearest 0.1ms. To add the extra significant figure, we used the expedient of multiplying our result by 10.

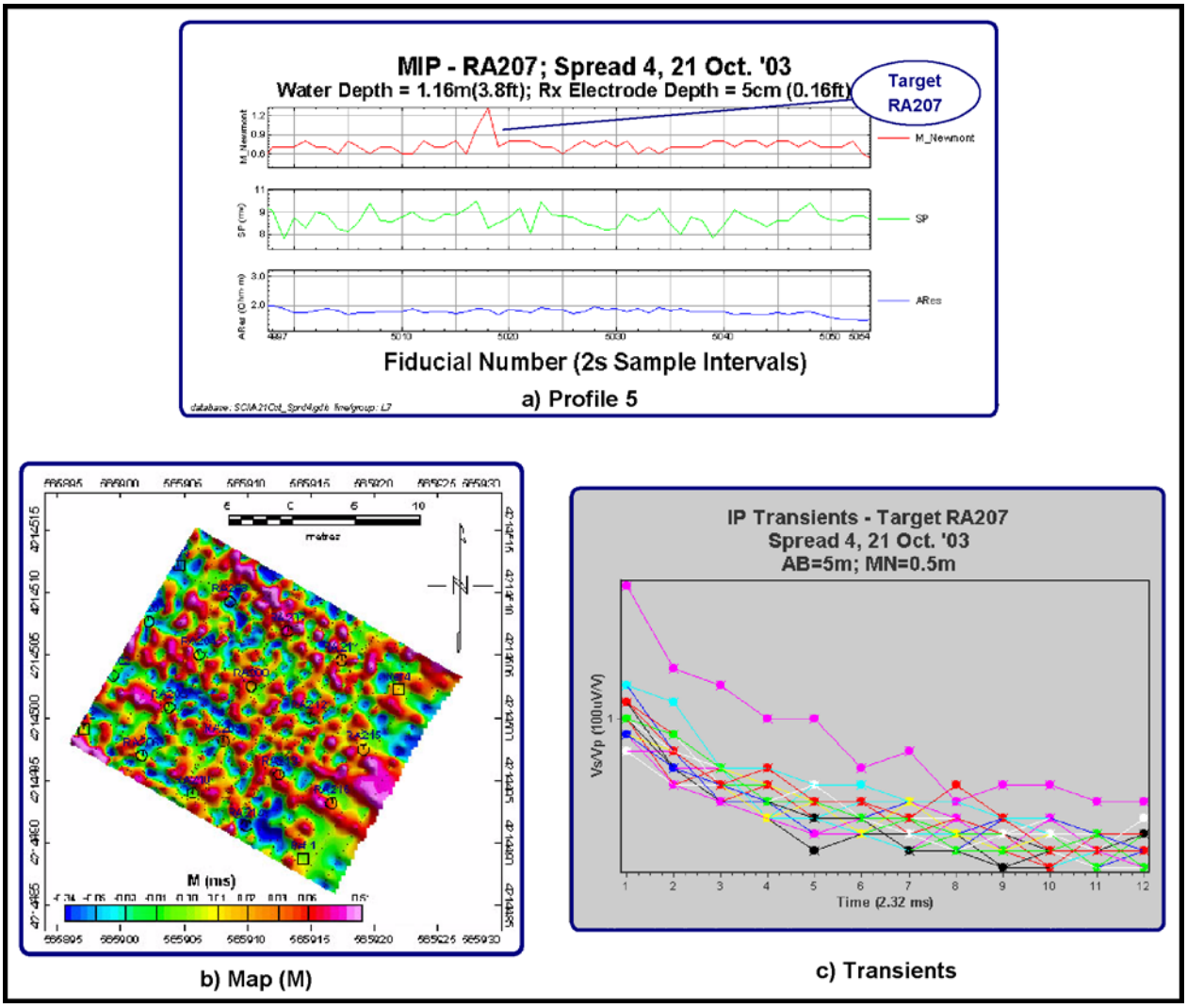

Figure 5.04: Composite figure showing center-line profile over target RA207 (a), color intensity map of leveled chargeability (M), and IP decay transients over target RA207 (c). Data are from Spread 4, water depth 1.16 m, Rx electrode depth 5 cm.

In addition to the chargeability (M), we plotted the differential SP, and the apparent resistivity (ARES) profiles in Figure 5.04a. The peak chargeability (M), centered at fiducial number 5018, correlates with target RA207. Note that there is no discernable expression of the target in either the SP or the apparent resistivity. The chargeability profile, M, however, shows that there are two problems with our data acquisition:

1. **Inadequate Sample Rate** – We were able to capture only 2 or 3 data points over RA207.
2. **Inadequate Resolution of M** – Poor resolution is not so apparent at this scale. However, when we look at the resolution of the IP data at an expanded scale, we note a distinct step-like behavior with a 0.1 ms granularity. As it happens, 0.1 ms is the least significant digit of the IP chargeability normally stored by the Zonge TDIP acquisition program. We repeated this survey after first lowering the electrodes to a depth of 55 cm beneath the water. We present those results as the composite Figure 5.07. In this figure, the data remain undersampled because we are acquiring 13-gate IP transients. However, because

the water level has dropped by approximately 30 cm and the electrodes are ½ m closer to the targets, the IP anomaly from target RA207 is at least twice as large.[18] As in the previous spread, the background noise in the chargeability (M) is less than the precision retained in our digital records.

Upon the completion of Spread 4, we lowered the 14 receiver electrodes to a depth of 55cm beneath the water surface and repeated the survey. Meanwhile, the tide was ebbing so that the water level dropped 12.5cm. The combination of a slightly lower water level together with receiver dipoles that were substantially closer to the water bottom produced much higher signal levels as we show in the summary plot in Figure 5.05. The figure corresponds one-for-one with

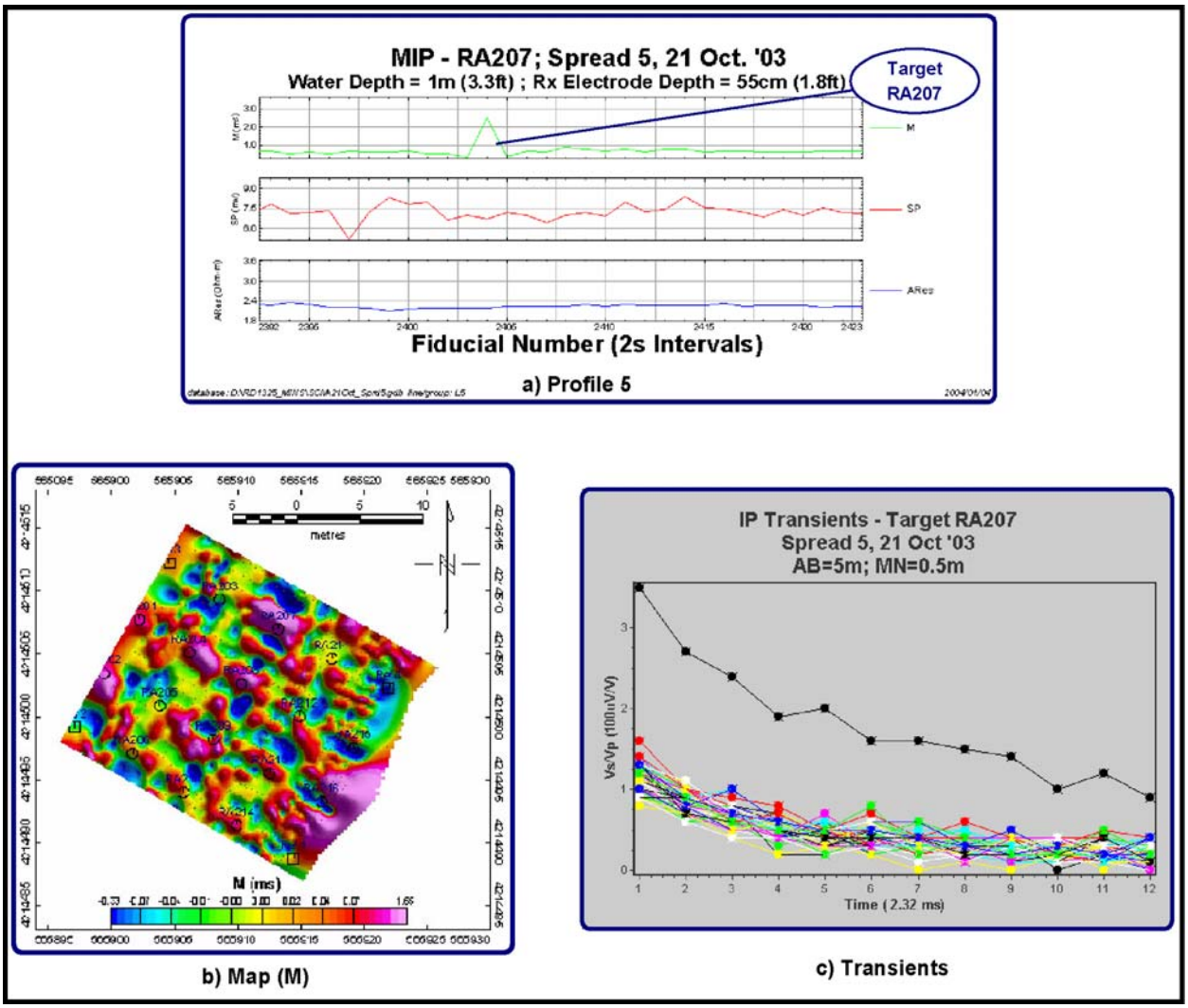

Figure 5.05: Composite figure showing center-line profile over target RA207 (a), color intensity map of leveled chargeability (M), and IP decay transients over target RA207 (c). Data is from Spread 5, water

[18] Because of the 2-sec sample rate, it is unlikely that we obtained an IP value at the peak of the anomaly from RA207 either on Spread 4 or Spread 5.

[19] Because of the 2-sec sample rate, it is unlikely that we obtained an IP value at the peak of the anomaly from RA207 either on Spread 4 or Spread 5.

the previous figure. Note the substantial increase in chargeability (a factor of approximately 3). In map view, target RA207 stands out well as does target RA208 adjacent to the southwest. Again, we can see from the chargeability profile (Figure 5.05a) that the anomaly field has been under-sampled and that the noise level in the chargeability is very low.

AB=5 m, MN= ½ m (Water Depth)

We obtained 4 additional spreads over the Reference Area on 21 October. These data sets were acquired with a version of our acquisition software that did not save the decay curves. Consequently, we were able to double our sample rate from 0.5 samples/sec to 1 sample per second. In addition, the tide continued to ebb while these surveys were being conducted. Therefore, the next sequence of maps shows a distinct improvement in the SNR of the chargeability maps due to both the progressively lower water levels and the higher sample rate.

The improvement in data quality brought about by the faster sample rate is better illustrated with profile data. In Figure 5.06, we show a profile similar to those we have shown in Figures 5.04a and 5.05a. The improvement in the data as the water level and hence the distance to the target diminishes, is evident from the chargeability maps generated from the 4 spreads (6-9) shown in Figure 5.07. We have plotted the sample points in these images to enable the reader to identify anomalies on the map that are just artifacts of the gridding process in areas of no data coverage.

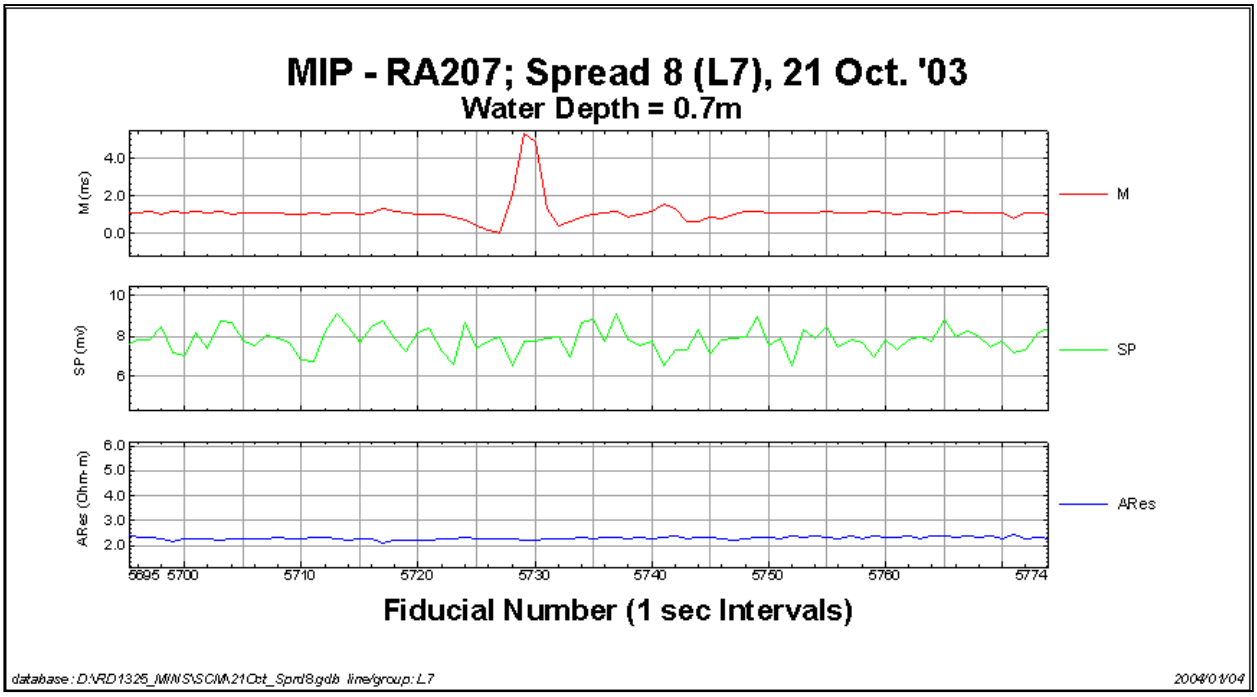

Figure 5.06: Center-line profile crossing target RA207. Sample rate = 1 sample/sec. RA207 is located at fid number 5729. A second anomaly (fid 5742) a much smaller amplitude correlates with RA208.

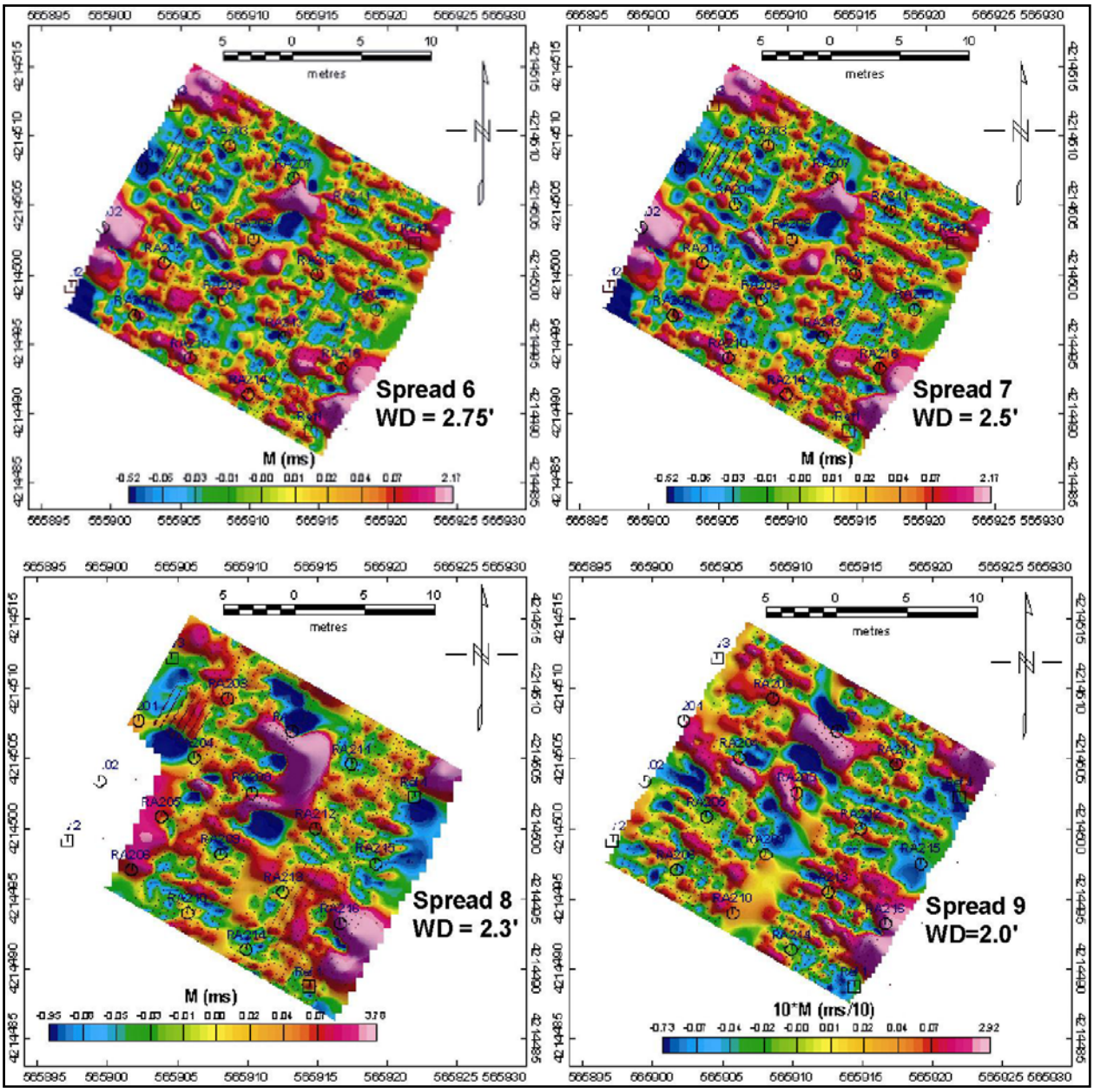

Figure 5.07: Sequence of 4 spreads illustrating progressive improvement in SNR as the water level decreases. AB = 5m, MN = 0.5m, Rx electrode depth = 55cm; sample interval 1s.

AB=10 m, MN= 1 m (Water Depth)

On our last survey day (24 October), we modified our electrode array so that the current electrode spacing (AB) was 10m and the receiver electrode spacing (MN) was 1m. We explained in Section 2 of this report that a longer AB spacing improves the depth of investigation. However, the signal level at MN drops and so we compensate for the loss in signal level by doubling the MN spacing. The net result is that while we improve our radius of detection for large targets, we reduce the sensitivity of the array for smaller targets. We acquired 4 spreads of time domain data using this array. The data were acquired with "fast" sampling (0.87sec sample interval). The results are displayed in Figure 5.08. In this sequence, the tide

was ebbing so each spread was acquired at a lower level then the preceding spread. Even with 1.5 m of water (upper left panel in Figure 5.08), target RA207 is well above the noise. The lower right panel in the figure (Spread 6) represents our only effort at acquiring data with profiles in the NW-SE direction. Turn-arounds were difficult on the NW side because of the proximity of the shore. However, we were able to map approximately ½ of the Reference Area in this direction at low water. It is interesting that the large anomaly over RA207 is diminished in amplitude and areal extent.[20] However, it appears that the anomaly immediately to the north of RA208 (presumably due to that target) now behaves much as the RA207 target did when we ran the survey with NE-SW survey lines.

[20] The positions of the anomalies in Spreads 5 and 6 appear to be systematically displaced from the plotted positions. This is a manifestation of the problems that we encountered with our GPS positioning versus the target coordinates provided – even when corrected by the same constant value for all data of our data sets.

5.4.2. Latency Tests

We mentioned earlier in this report that we performed several latency tests in an effort to determine the correction between the times that are stored in the GPS data logger and those that are stored with our IP data. On land, a latency test is easy to perform by surveying back and forth over a target at a known position. It is not so easy to perform the same test in shallow water subject to winds and strong currents. Our main problem was in the navigation to a point within less than a meter. We tried two types of latency tests:

1. Repeated passes over a planted target laying "proud" on the water bottom
2. Repeated passes over target RA207

Figure 5.09: 60 cm (2 ft) piece of box structural steel used in "proud" latency test.

Proud Target Latency Test – This test emulates tests we conduct periodically with electromagnetic induction (EMI) systems used for UXO detection. We found a 60 cm length of heavy box-shaped structural steel (Figure 5.09), tied it to a small mooring buoy and placed it in shallow water. Then we made repeated survey passes in opposite directions over the buoy. One problem with this approach is that it was very difficult for us to obtain a measurable anomaly

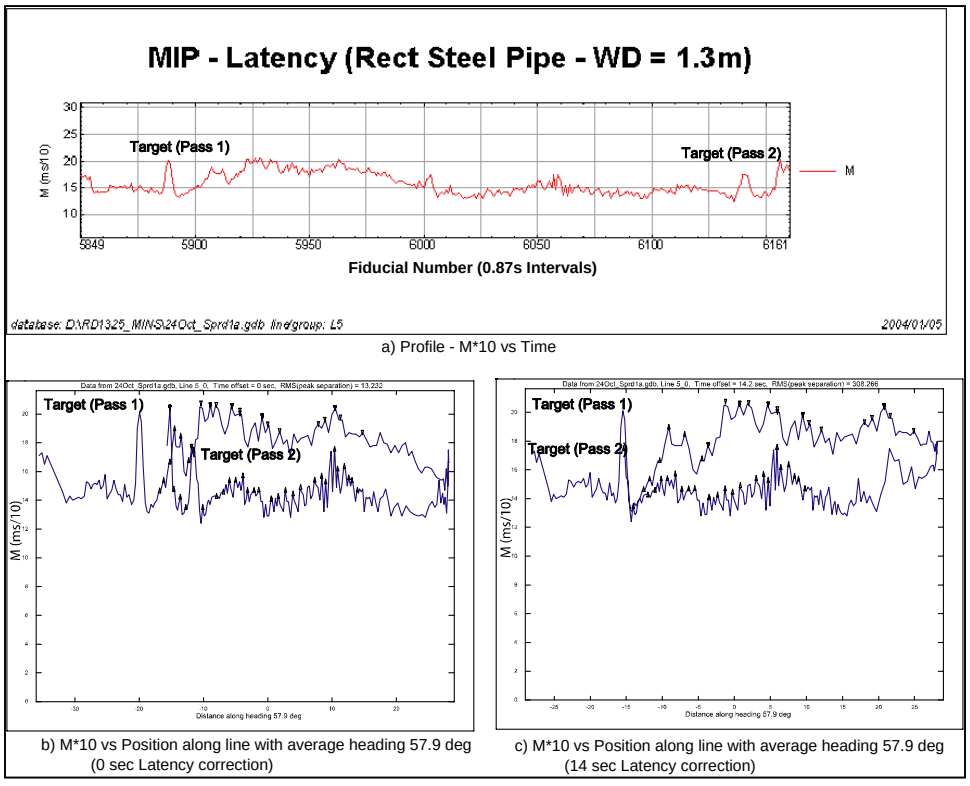

Figure 5.10: Summary diagram of latency test using 2-ft length of steel (shown in Fig. 5.09). The results show a timing correction of 14s is required.

from the target for the same dipole pair on adjacent passes.[21] We tried several times to obtain a good latency test, but we succeeded only once in obtaining responses from adjacent passes over the target. We present the results of this latency test in Figure 5.10. The top figure (5.10a) shows the profile that we acquired plotted as a function of the fiducial number.[22] The lower left hand figure (5.10b) is a plot of the chargeability versus a distance along a profile in the direction 57.9° (i.e., the mean orientation of the profile as computed from GPS positions) with no timing (latency) correction applied. That figure shows an offset between the two anomaly peaks identified in Figure 5.10a. Figure 5.10c plots the same data after applying a 14 sec time correction to the GPS data. The two anomaly peaks are now aligned as expected.

A remarkable thing about these data is that they were acquired in more than 1.3m of water under difficult conditions (current, wind, and wave action). The peak target anomaly is very small (~0.5ms = 5 ms/10) and yet the anomalies are easily discernable from low-level with short wavelengths and longer wavelength noise with approximately the same amplitude as the anomalies. The long period variation in the chargeability profile (with amplitude of about 0.5 ms between fid no's 5900 and 6000) is certainly the result of maneuvering during the turn-around for the pass in the reverse direction. After fid number 6000, the chargeability settles back to 1.5ms (15 units), about the same as it was when approaching the target from the opposite direction (between fid numbers 5948 and 5985).

Target RA207 Latency Test – We alluded to the problems encountered in successfully conducting the latency test described above. Those data were acquired on 24 Oct. However, we were aware that we had a problem with latency after reviewing the data we had acquired on 21 Oct, 3 days earlier. In all of our tests, however, we always detected an anomaly over target RA207, regardless of tide level. So we decided to use RA207 as a target for latency tests. On 23 Oct, we spent approximately 15 minutes running NE-SW profiles back and forth over column 3 of the Reference Area (see Figure 5.02) passing over target RA207. We made 3 round trip passes in relatively low water (~0.6 m). As we see from Figure 5.11a, we crossed RA207 with our number 4 (center) dipole on 5 of the 6 passes. When the correct timing correction (14 sec) is applied and we plot the profile as a function of the UTM northing coordinate of the data points (Figure 5.11b), the 5 peaks overlay, again demonstrating proper correction and merging of GPS positions.

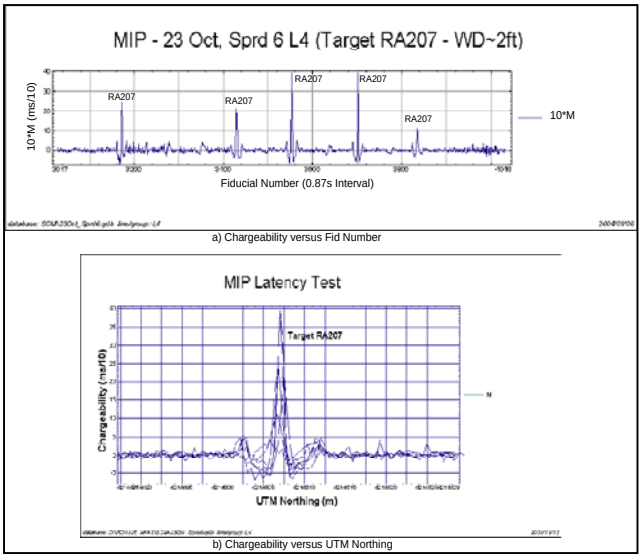

Figure 5.11: Latency check – Multiple passes over target RA207.

[21] All measurements were made within a few hours of low tide. We had to battle strong currents, large wakes from Mare Island Channel traffic (ferries and freighters), and at times strong winds. It was difficult to tow our electrode array and cross the target within ±1m.

[22] When we acquired this data, we were using yet another version of the TDIP acquisition software. In this version of TDIP, the sample rate was 1.14 samples/sec (8 Hz base frequency, 2 cycle stack). Chargeability values were multiplied by 10 (i.e., 10*M) thereby providing us an extra decimal digit of resolution.

5.4.3. Target Parameterization

We can use the dipole model to fit models to data acquired over anomalies in the Reference Area. To illustrate, we have taken the profile data shown in Figure 5.11 for target RA207 and fit it with a polarizable model in an otherwise uniform half-space. In this example, we have incorporated the 4-electrode gradient array geometry (10m AB, 1m MN) and we have assumed that the profile runs directly over the model. We present the results of the model fit in Figure 5.13. The observed data shown in the figure are the data points from the 6 profiles shown in Figure 5.11. The fact that these profiles are not actually coincident explains the scatter. But it is interesting that by modeling the electrode array geometry, we were able to capture the complex structure of the anomaly as the electrodes pass over the target. The depth of the target has been underestimated. In this case, the water depth was about 61 cm (2 ft) and the target (RA207) is reported to lie at 60 cm beneath the bottom.

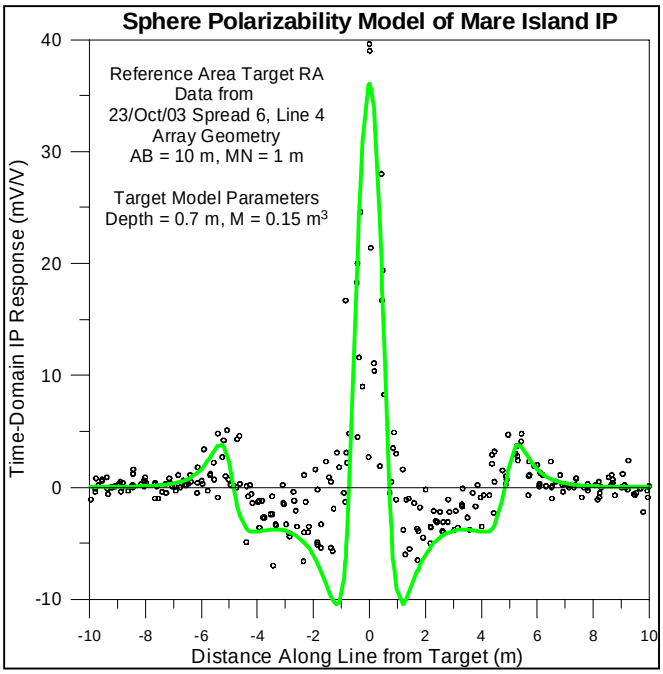

Figure 5.12: Isotropic dipole model fit to the profile data shown in Figure 5.11 for target RA207.

5.4.4. Frequency Domain

Complex Resistivity (CR) Measurements (AB = 5m, MN= ½ m)

We acquired complex resistivity (CR) spectra from both a background situation and with our electrode array held in a (more or less) static position over target RA207. We present those results as a composite plot in Figure 5.13. These spectra have been compiled from Fourier analyses of the first 5 odd harmonics generated from a square wave current source, at fundamental frequencies of 0.125, 1.0, and 8.0 Hz.

The background spectrum (blue curves) was measured while "holding station" in deeper water against tide and wind. Note that the amplitude is constant over nearly 3 decades while the phase remains close to 0 mr out to

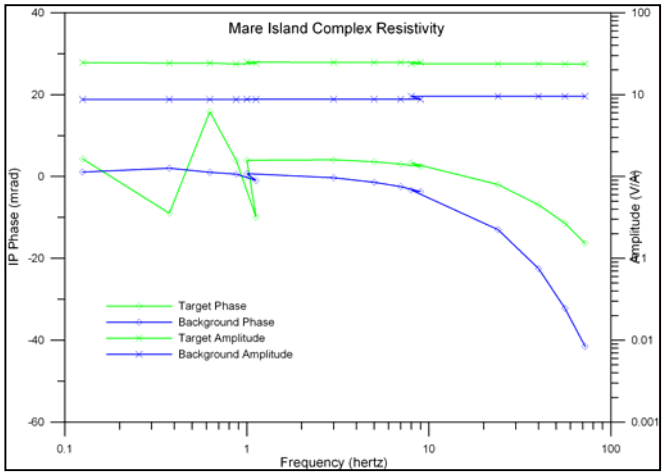

Figure 5.13: Complex resistivity spectra acquired over background (blue), and target (green) at Mare Island.

8 Hz after which it starts to become increasingly negative (-40 mr at 72 Hz). This behavior is consistent with electromagnetic coupling. Consistent with our model studies, we see that the electromagnetic coupling, in this case, can be neglected out to about 8 Hz. At higher frequencies the EM coupling becomes large and negative.

We measured the CR spectra over target RA207 at near low tide. We attempted to hold our electrodes over the peak of the anomaly by tightly securing at each end of the bridal on our electrode array. However, we were not entirely successful as can be seen by examining the green curves in Figure 5.12. The segment of the phase curve from 0.125 Hz to 1.125 Hz (i.e., the 9^{th} harmonic of 0.125) is noisy and obviously does not fit together with the smooth curve generated by the harmonics from the two higher fundamental waveforms (1 Hz and 8 Hz). We believe that the noise is due to wave motion produced by waves.[23] On the green curves, note that the shape of the amplitude curve is the same as the background but has a higher level. The higher amplitude indicates higher apparent resistivity. Generally speaking, the resistivity is primarily affected by the water depth for these short arrays. Thus, the difference in the amplitude values in the two spectra in Figure 5.12 suggest that the water depth at the target site is less than the water depth at the background site, as indeed was the case. The target phase curve has been shifted positive with respect to the background curve. At 1 Hz, the target exhibits a 5 mr phase shift that is fairly constant with frequency until about 8 Hz, after which it starts to fall off in a manner consistent with that of EM coupling.

We make the following conclusions from these CR spectra: 1) EM coupling can be safely neglected up to 8 Hz (for AB = 5m) and at higher frequencies can be treated as a constant background (provided the water depth does not change rapidly over the area of interest), and 2) the uniform CR phase response of the RA207 target at low frequencies suggests that the IP response of the target is characterized by a broad distribution of time decays. There is no suggestion from these data that targets may have characteristic spectral shapes or time decays.

[23] Even on land, good measurements at 0.125Hz are sometimes hard to acquire because we need to stack 4-8 cycles of the fundamental to get reliable phases. It therefore takes 32 to 64 sec to acquire the data.

6. Conclusions and Recommendations

6.1 Conclusions

1. Laboratory experiments and numerical modeling demonstrate that a measurable IP response is associated with metallic objects submerged in an aqueous electrolyte. Targets in a saltwater solution generate a significantly higher IP response than equivalent targets in freshwater.

2. Using calibrations based on our laboratory measurements, numerical models of field-scale scenarios indicate the following: 1) the depth to target and dipole size should be on the order of the size of the target (long dimension); 2) short AB-gradient or Ladder arrays produce the best combination of signal strength and IP response; 3) target orientation is significant; and 4) EM coupling is insignificant for the relatively small scale arrays and low frequencies (<8 Hz) used for a marine IP/UXO survey.

3. The full-scale field experiment was a "qualified" success. It is clear from the results that the UXO generate a measurable IP response. But targets seeded in the MINS Reference Area were not easily detected with the surface electrode array that we deployed. In part, this was due to inadequacies in our experimental apparatus. Our laboratory and numerical experiments clearly indicate, for example, that the detection of small targets (e.g., RA211-RA216) requires a small receiver dipole size (i.e., 0.25m or smaller). Moreover, the range of detection is a function of dipole size and probably is no more than 3-5 dipole lengths. It is not surprising therefore, that we did not detect the small targets. A second problem was with the inadequate sampling rate (0.87s/sample max). Only one of the test targets (RA207, a 5" 54 projectile, horizontal orientation parallel to the line/primary field, sub-bottom depth 0.61 m) was clearly detected on all of the test runs using the MN/AB = 5m/0.5m dipole sizes (sea bottom-Rx separations ranged from 0.5 to 1.11 m). The nose-down equivalent of RA207 is target RA203, which was not detected on any of the test passes. However, this target was buried at a depth of 1.2m. One other target anomaly was detected, with less confidence, on some of the tests (RA208, a 3" 50 cartridge, horizontal orientation parallel to line/primary field, sub-bottom depth 0.61 m). When surveying along NE-SW traverses, we were unable to maneuver our electrode array to pass over these targets because of the boundary marker posts (Figure 5.01). Ideally, this target would have been best detected with traverses in the NW-SE directions. But as we have said, we were unable to successfully maneuver our array between the shore and the boundary of the reference area.

4. For the MN/AB = 10m/1m dipole size trials at MINS, again only target RA207 was clearly detected, although no clear anomaly was observed for it on the single test using a NW-SE (cross-line) traverse/primary field direction. At this array scale, this target is still clearly detectible from the surface in 1.5m (5ft) of water. The map data in shown in Figure 5.07 clearly has benefited from a marginally improved sample rate and multiple coverage in some areas that provided a greater density of sample points for map generation.

5. As predicted, the MINS field test indicates that both target orientation and target/Rx dipole separation are significant detection factors. Longitudinal targets (having their long axes aligned in the direction of the primary field) have higher S/N anomalies than transverse targets.

6. We were pleasantly surprised with the very low IP noise levels we encountered during our experiments at Mare Island. With noise levels on the order of 0.1ms, anomalies as small as 0.5ms are easily detectible.

6.2 Recommendations

We are cautiously encouraged by the results of our Mare Island experiment. With hindsight, there are a number of things we might have done differently to improve our results. The main problem was in finding a suitable test site at which to conduct controlled experiments. At Mare Island, experiments were compromised by the difficulties from strong tidal currents, winds, and sometimes wakes generated by ferries and other large vessels passing through the Mare Island Strait. These factors, coupled with the need to maneuver a towed electrode bridal cable approximately 20m long inside an area with the same dimension made it difficult to position the array accurately. Should this work be continued, we need to find a shallow test lagoon not subject to strong currents and winds. We are aware that such test sites exist within the U.S. Naval Facilities and that it will be necessary to make contact with Naval personnel managing a suitable facility and request access for test purposes.

Our experience at Mare Island has definitely permitted us to identify important improvements to our experimental apparatus so that any future experiments will be more conclusive. We enumerate those improvements below and offer them as recommendations that would be the focus of any subsequent follow-on work:

1. ***Submerged Electrode Array*** – Both our laboratory and field experiments have confirmed that the range of detection of the IP effect from single objects must be expressed in units of receiver dipole lengths (MN). Moreover, small MN spacings are required for the detection of small targets. Assuming a properly scaled electrode array, the range of detection is at best 2-4 dipole lengths. If we are to detect a range of target sizes, it is imperative that the electrode array be submerged to a depth as close to the bottom as possible.

2. ***Multiplexed Electrode Array*** – Both our laboratory and field experiments have confirmed that the range of detection of the IP effect from single objects must be expressed in units of receiver dipole length (MN). Moreover, small MN is required for the detection of small targets. It is clear to us, therefore, that in order to detect a range of targets sizes, it will be necessary to survey with at least 2 receiver dipole sizes. Furthermore, our results have indicated a very strong anisotropy in the response with the largest response coming when the target is polarized by an electric field that is parallel with its longitudinal axis. This suggests either that we survey an area in two directions or that our electrode array include two mutually orthogonal transmitter dipoles (AB's) that are multiplexed between readings. At a 5m scale, such an arrangement seems achievable, particularly in shallow water. In any case, input channels must be multiplexed between a set of larger MN dipoles (e.g. 1m/0.5m) that will be sensitive to the presence of large targets and a set of smaller dipoles (e.g. 15/30cm) that will be sensitive to smaller targets.

3. ***Data Acquisition System*** – It is clear that if IP detection of mines and UXO is to be practical, it will require the simultaneous measurements of as many receiver dipoles as practical. Our 8-channel receiver (1 current monitor, 7 receiver dipoles) demonstrated that it is practical to have a measurement footprint as wide as 3m. However, as we have indicated in the previous recommendation, it is highly desirable, if not absolutely necessary that we measure response at two different scales. Ideally, this will require an acquisition system with many more channels. Together with a multiplexing scheme, we believe that a system with 32 receiver dipoles is practical. Even more important than channel capacity, however, is the ability to acquire data at a high report rate. At base frequencies of 8 Hz or perhaps even 16 Hz, it will be necessary to store an IP response at the base frequency rate (8 samples/sec or 16 samples/sec). For a multiplexed array, the base frequency can be safely increased when measuring from smaller electrode arrays (e.g., 5m AB / 0.25 MN) without creating problems with EM coupling. And as we go to smaller arrays, there is a requirement for higher sampling rates.

4. ***Navigation System*** – There are special requirements placed on a navigation system that can effectively recover the position of each of the individual electrodes. In very shallow water (e.g. < 2m), it is practical to fix a GPS antenna to a submerged electrode sled that protrudes, periscope-like, above the water. However, we will be dealing with a rather large electrode array, perhaps as large as 3m in the transverse direction. Therefore, it will be necessary to track the attitude (i.e., heading, pitch, and roll angles) of the electrode sled in order to recover the measurement positions of all of the measurement dipoles. Our experience in operating the towed electrode array in the tidal currents and cross-winds at Mare Island provided us with graphic visual evidence of how severely the electrode array can be "crabbed" with respect to our course-made-good. With an underwater electrode array, the problem is magnified since there are 3 attitude angles that may vary significantly as the array is towed along. It will also important to record depth from the electrode platform to the water bottom.

5. ***Data Processing & Interpretation*** – As we are presently learning with regard to dealing with multiple receiver EMI arrays, a system for the reduction and presentation of these data is quintessential for the demonstration of the technology. We have a simple model for the response of the target (i.e., an anisotropic point dipole). Our multi-channel data acquisition system (including, perhaps, multiplexed receiver electrodes and transmitter electrodes) allows us to sample in 1 spatial dimension (transverse to direction of motion). The platform motion itself provides the second dimension. The data that we are able to acquire by towing the array provides the opportunity to perform what could be termed electrical impedance tomography (EIT). One of our collaborators (LaBrecque) has considerable experience in applying EIT using static electrode arrays on land.

7. References

1. Swift, C.M.J., *The L/M parameter of time-domain IP measurements - A computational analysis.* Geophysics, 1973. **38**(1): p. 61-67.
2. Bertin, J., and J. Loeb, *Experimental and Theoretical Aspects of Induced Polarization*. 1976, Berlin: Gebruder Borntraeger.
3. Sumner, J.S., *Principles of Induced Polarization for Geophysical Exploration*. 1976, New York: Elsevier Scientific Publishing Company. 277.
4. Grow, L.M., *Induced Polarization for Geophysical Exploration*, in *The Leading Edge*. 1982. p. 55-56,69-70.
5. Bleil, D.F., *Induced polarization: A method of geophysical prospecting.* Geophysics, 1953. **18**: p. p. 636-661.
6. Brant, A.A., *Historical Summary of Overvoltage Developments by Newmont Exploration Limited, 1946-1955*, in *Overvoltage Research and Geophysical Applications*, J.R. Wait, Editor. 1959, Pergamon Press: London.
7. Graeme, D.C., *Mathematical theory of faradaic admittance.* Electrochemical Soc. Jour., 1952. **99**: p. 370C-384C.
8. Stratton, J.A., *Electromagnetic Theory*. 1941, New York: McGraw-Hill Book Company, Inc. 615.
9. Keller, G.V., and Frank C. Frischknecht, *Electrical Methods in Geophysical Prospecting*. 1 ed. 1966, New York: Pergamon Press. 519.
10. Wait, J.R., *Geo-Electromagnetism*. 1982, New York: Academic Press.
11. Abramowitz, M., and Irene A. Stegun, *Handbook of Mathematical Functions*. Fourth ed. 1964, Washington, DC: U.S. Government Printing Office. 1046.
12. Alloud, L.A., and Maurice H. Martin, *Schlumberger, The History of a Technique*. 1977, New York: John Wiley & Sons. 333.
13. Sunde, E.D., *Earth Conduction Effects in Transmission Systems*. 1949, New York: D. Van Nostrand Co.
14. Ward, S.H., and Gerald W. Hohmann, *Electromagnetic Theory for Geophysical Applications*, in *Electromagnetic Methods in Applied Geophysics - Theory*, M.N. Nabighian, Editor. 1987, Soc. Explor. Geophys.: Tulsa. p. 513.
15. Marshall, D.J., and T.R. Madden, *Induced polarization: A study of its causes.* Geophysics, 1959. **24**(4): p. 790-816.
16. Maung, T.U., *Measurement of induced polarization with variation of water saturation in core samples*, in *Geophysics*. 1960, Colorado School of Mines: Golden, CO.
17. Wong, J., *An electrochemical model of the induced-polarization phenomenon in disseminated sulfide ores.* Geophysics, 1979. **44**(7): p. 1245-1265.
18. Frische, R.F., and Haro von Buttlar, *A theoretical study of induced polarization.* Geophysics, 1957. **22**(3): p. 688-706.
19. Wait, J.R., *Discussion on 'a theoretical study of induced electrical polarization'.* Geophysics, 1958. **23**(1): p. 144-153.

20. Slayter, L.D., and D. Lesmes, *IP interpretation in environmental considerations.* Geophysics, 2002. **67**(1): p. 77-88.
21. Seigel, H.O., *Mathematical formulation and type curves for induced polarization.* Geophysics, 1959. **24**(3): p. 547-565.
22. Coggon, J.H., *A comparison of IP electrode arrays.* Geophysics, 1973. **33**(4): p. 737-761.
23. Barker, R.D., *Depth of investigation of collinear symmetrical four-electrode arrays.* Geophysics, 1989. **54**(8): p. 1031-1037.
24. ECC, *Validation of Detection Systems (VDS) Test Program Final Report*. 2000, Environmental Chemical Corportation: Burlingame, CA. p. 44.

8. List of Figures

Appendix A Documented Data Set Description

A.1 Data File List and Definitions

File Name	*Extension*	*Description*
		21-Oct-03
Mins_21Oct	nts	Notes on 21/Oct/03 data acquisition and processing
Mins_21Oct	raw	unsplit 21/Oct/03 GDP32 raw data
21Oct_Sprd4	raw	21/Oct/03 GDP32 raw data
21Oct_Sprd5	raw	"
21Oct_Sprd6	raw	"
21Oct_Sprd7	raw	"
21Oct_Sprd8	raw	"
21Oct_Sprd9	raw	"
21Oct_Sprd4	cfg	21/Oct/03 TDIP survey configuration files
21Oct_Sprd5	cfg	"
21Oct_Sprd6	cfg	"
21Oct_Sprd7	cfg	"
21Oct_Sprd8	cfg	"
21Oct_Sprd9	cfg	"
21Oct_sprd1-3	gps	21/Oct/03 gps location csv files
21Oct_sprd4	gps	"
21Oct_sprd5	gps	"
21Oct_sprd6	gps	"
21Oct_sprd7	gps	"
21Oct_sprd8	gps	"
21Oct_sprd9	gps	"
21Oct_Sprd4	gdb	21/Oct/03 TDIP in Oasis montaj data base
21Oct_Sprd5	gdb	"
21Oct_Sprd6	gdb	"
21Oct_Sprd7	gdb	"
21Oct_Sprd8	gdb	"
21Oct_Sprd9	gdb	"
		22-Oct-03
Mins_22Oct	nts	Notes on 22/Oct/03 data acquisition and processing
Mins_22Oct	raw	unsplit 22/Oct/03 GDP32 raw data
C102215A	gps	unsplit 22/Oct/03 gps location csv files
C102215b	gps	"
C102216A	gps	"
22Oct_sprd6	raw	GDP32 raw data, 22/Oct/03 spread 5, TDIP + CR data
22Oct_sprd5-CR	raw	CR data from 22/Oct/03 spread 5
22Oct_sprd5-TD	raw	TDIP data from 22/Oct/03 spread 5, used to locate target RA
22Oct_sprd4	raw	GDP32 raw data, 22/Oct/03 spread 4
22Oct_sprd4	cfg	TDIP configuration file

22Oct_sprd4	gps	gps location csv file
22Oct_sprd4	gdb	Oasis montaj data base
22OctCR	raw	GDP32 raw data, CR from spread 5 = 22Oct_sprd5-CR.raw
22OctCR	mde	Data processing control and annotation
22OctCR	avg	CR data in a tabular ASCII format, 22/Oct/03 spread 5
		23-Oct-03
Mins_23Oct	nts	Notes on 23/Oct/03 data acquisition and processing
Mins_23Oct	raw	unsplit 23/Oct/03 GDP32 raw data
C102314A	gps	unsplit 23/Oct/03 gps location csv files
C102316A	gps	
23Oct_Sprd6	raw	23/Oct/03 GDP32 raw data, spread 6
23Oct_Sprd6	cfg	TDIP configuration file, spread 6
23Oct_Sprd6	gps	24/Oct/03 gps location csv file, spread 6
23Oct_Sprd6	gdb	Oasis montaj data base, spread 6 TDIP
		24-Oct-03
Mins_24Oct	nts	Notes on 24/Oct/03 data acquisition and processing
Mins_24OctA	raw	unsplit 24/Oct/03 GDP32 raw data, part A
Mins_24OctB	raw	unsplit 24/Oct/03 GDP32 raw data, part B
24Oct_Sprd1	raw	24/Oct/03 GDP32 raw data, split by spread
24Oct_Sprd2	raw	"
24Oct_Sprd3	raw	"
24Oct_Sprd4	raw	"
24Oct_Sprd5	raw	"
24Oct_Sprd6	raw	"
24Oct_Sprd3	cfg	24/Oct/03 TDIP survey configuration files
24Oct_Sprd4	cfg	"
24Oct_Sprd5	cfg	"
24Oct_Sprd6	cfg	"
24Oct_Sprd1	gps	24/Oct/03 gps location csv files
24Oct_Sprd2	gps	"
24Oct_Sprd3	gps	"
24Oct_Sprd4	gps	"
24Oct_Sprd5	gps	"
24Oct_Sprd6	gps	"
24Oct_Sprd1	gdb	24/Oct/03 TDIP data, Oasis montaj gdb files
24Oct_Sprd3	gdb	"
24Oct_Sprd4	gdb	"
24Oct_Sprd5	gdb	"
24Oct_Sprd6	gdb	"
24OctCR	raw	CR data = 24Oct_Sprd2.raw
24OctCR	mde	CR data processing control and annotation
24OCTCR	avg	CR data in tabular ascii format

		25-Oct-03
Mins_25Oct	nts	Notes on 25/Oct/03 data acquisition and processing
NTF26171	cac	GDP32 TEM data binary output file
NTF26171	cfg	TEM system configuration file
C102510a	gps	Unsplit 25/Oct/03 gps data
ntf26171	gdb	Oasis montaj data base of TEM data

A.2 Data File Format Descriptions

GPS Files: GPS time and geographic coordinate data

GPS location data were saved to tabular ascii files with a comma-separated-value (csv) format with columns of:

Date	Date (dd/mm/yy)
Time	Time (hh:mm:ss)
GridEast	Easting (m)
GridNorth	Northing (m)
Elev	Elevation (m)
Feature_num	Feature number (GPS acquisition category index)
Feature_type	Feature type (GPS acquisition category)
Feature_name	Name corresponding to TDIP "spread"
PDOP	Precise Dilution of Precision (dimensionless, ideal PDOP is <7)
Corr_stat	Type of GPS error statistics
Horz_err	Horizontal error estimate (m)
Vert_err	Vertical error estimate (m)

GDB Files: TDIP data in Oasis montaj data base files

Files with the extension gdb are in a proprietary Geosoft Oasis montaj data base format. Working with data in gdb files requires either the Oasis montaj software package, although reading gdb files is possible with a free viewer available from the Geosoft web site, www.geosoft.com.

TDIP data from this project were stored in gdb with columns of:

Ares	gradient array apparent resistivity (ohm-m)
GDP_Blk	GDP raw-file block number
GDP_Time	GDP time of day (hh:mm:ss.s)
Heading	(deg cw of North)
Line	Line number, used to identify Rx dipole (1 to 7)
Line_Distance	Distance along line (m)
M_Newmont	Modified Newmont chargeability (msec)
M_Newmont_Flt	Newmont chargeability with background offset removed (msec)
M_Trans[0:11]	TDIP transient (mV/V)
Merr	Estimated Newmont chargeability error (msec)
RxLen	Rx dipole length (m)
SP	SP offset (V)
TxAmp	Tx current (A)
TxFreq	Tx frequency (hertz)
TxLen	Tx bipole length (m)
Vp	Peak voltage (V/A)

X GPS Easting (m)
Y GPS Northing (m)
Z GPS Elevation (m)

TDIP RAW Files: GDP32 time-domain IP raw data

Raw TDIP data are stored in Zonge block-formatted ASCII data files. An excerpt from a TDIP RAW file follows:

```
0072
TDIP0530 92-09-22 14:55:34 13.7v D-D
Tx        1 Rx        3 N OUT   ESys 1.000
.500 Hz      1 Cyc Tx Curr     1
1  ON     1  -1.4992u   210.2 -2.826m 026O   0.00   -0.28     0  0
2  ON     2  -1.3321u   -42.6 -10.04m 026O   0.00    0.00     0  0
3  ON     3  -3.1433u     5.8 -59.25m 026O   0.00    0.00     0  0
Windows
    1       2       3       4       5       6       7       8
      1      -1  982595
   3199   -5614   -1252
   5457     317    5474
  -5833   -5084    -649
   6115   -1588     788
   4234   -4554    1763
  14678    5084   -4036
   6680   -8474   -3340
   5645   -4660    2319
   5080     423   -3340
   3010    1906    2134
   4610    -423   -3572
  11667   -3283   -5428
...
```

The lines in the RAW file are defined as follows:

Line 1
Block Number

Line 2
Survey Type
Version Number
Skip Flag
Date
Time
Voltage
Array Type

Line 3
Tx value
Rx value
Notch value
Int/Ext System
Calibrate Voltage

Line 4
Frequency
Cyc value
Tx Current

Line 5-7 (repeated for each channel measured)
Channel Number
Skip Flag
Channel Type
N-Spacing
Primary Voltage
Chargeability
Resistivity
Gains/Attenuator
SEM
Self Potential
Contact Resistance
External Amp Gain

Line 8-9 Window header lines

Line 11-24 TDIP input data file window structure

CR RAW Files: GDP32 frequency-domain complex resistivity IP raw data

Raw CR data are stored in Zonge block-formatted ASCII data files. An excerpt from a CR RAW file follows:

```
0011
CR  0530 93-07-04 16:05:29 12.8v D-D
Tx        1 Rx        5 N OUT   ISys 1.000
   1 Hz     16 Cyc Tx Curr     1
1  Ex     1   1.2729  -1570.8  78.51K 000O   0.00   -0.41     0  0
2  Ex     2   1.2726  -1570.3  78.40K 000O   0.00   -0.14     0  0
3  Ex     3   1.2731  -1570.6  78.15K 000O   0.00    0.00     0  0
4  Ex     4   1.2727  -1570.3  77.65K 000O   0.00   -2.20     0  0
5  Ex     5   1.2722  -1570.6  76.98K 000O   0.00    0.00     0  0
Harmonics 1               3               5               7 ...
1  1.2729  -1727.0  415.65m -2038.9  239.38m -2350.1  160.63m  ...
2  1.2726  -1729.6  414.70m -2046.2  237.97m -2360.3  159.03m  ...
3  1.2731  -1728.2  415.31m -2042.4  238.77m -2355.4  160.05m  ...
4  1.2727  -1726.3  415.06m -2036.5  238.54m -2344.5  159.72m  ...
5  1.2722  -1729.4  414.92m -2045.7  238.36m -2360.3  159.47m  ...
...
```

The lines in the CR RAW file are defined as follows:

Line 1
Block Number

Line 2
Survey Type
Version Number
Skip Flag
Date
Time
Voltage
Array Type

Line 3
Tx value
Rx value
Notch value
Int/Ext System
Calibrate Voltage

Line 4
Frequency
Cyc value
Tx Current

Line 5-9 (repeated for each channel measured)
Channel Number
Skip Flag
Channel Type
N-Spacing
Fourier Magnitude
3-Point DC Phase
Resistivity
Gains/Attenuator
SEM
Self Potential
Contact Resistance
External Amp Gain

Line 10 Harmonic data header line

Line 11-15 Harmonic Data Lines:
Channel Number
Magnitude Harmonic 1, Phase Harmonic 1
Magnitude Harmonic 3, Phase Harmonic 3
Magnitude Harmonic 5, Phase Harmonic 5
Magnitude Harmonic 7, Harmonic Phase 7
Magnitude Harmonic 9, Harmonic Phase 9

CR MDE Files: CR data processing control and annotation

The following variable names are recognized in a Zonge ASCII .MDE file by the CRAVG data processing program:

COMPANY Company name
CLIENT Client name
PROJECT Project name
JOBNUMBER Company job number
JOBDATE Survey date
JOBLINE Survey line number
BRGLINE Line forward bearing
BRGBACK Line back bearing
STNLOW Low station number, plot limit
STNHIGH High station number, plot limit
STNDELT Station number increment, plot scale
LBLFRST Low station number, axis label
LBLDELT Station number increment, axis label
FRQLO Low frequency, plot limit
FRQHI High frequency, plot limit
RXBRG Receive dipole bearing, usually same as survey line orientation
PLTREV Plot X-axis reverse selection
UNITS Units for listed values, such as A-Spacing. Feet or meters.
AUTO Run program without prompts
FMIN Reference frequency for calculation of Resistivity and decoupled phase
FMAX Unusable high frequency values can be ignored.
HARMONIC Limit the maximum harmonic to be processed.
GAIN Adjust for changes of Receiver gains or Transmitter current at each data point.
DFILE Averaged data may be written to a data file for use by other programs.

ZFILE	The averaged data may be written to a plot data file for use by other programs.
PAUSE	Mode PAUSE interrupts screen plots before the plot is overwritten by text.
HELP	Verbose prompts
ERRORBARS	Error bars are available for averaged magnitude data only.

CR AVG Files: tabular columns of CR data

CR AVG files are ASCII column-delimited files containing averaged CR data. An excerpt from a CR .AVG file follows:

```
\ CRAVG 7.20: "SAMCR.FLD", Dated 91-09-20, Processed 02 Aug 93
$ ASPACE= 200.0m
\ 0.Hz Mag= RhoA @  0.125 Hz, Phz= 3-Pt Phz @ .125,.375,.625 Hz
skp     Tx      Rx    PltPt    NSp  Freq Cmp Amps  Resistivity Phase    Real      Imag      %Rho   sPhz
\-++------++------++------++----++----++-++----++---------++------++---------++---------++-----++-----+
 2     6.00    2.00    4.50   3.0 0.000 Ex  0.    9.6052e+1    4.3  1.0000e+0  0.0000e+0    0.0    0.1
 2     6.00    2.00    4.50   3.0 .1250 Ex  1.9   3.2440e-3    3.8  1.0000e+0  3.8000e-3    0.0    0.0
 2     6.00    2.00    4.50   3.0 .3750 Ex  1.9   3.2338e-3    3.5  9.9685e-1  3.4890e-3    0.0    0.2
 2     6.00    2.00    4.50   3.0 .6250 Ex  1.9   3.2310e-3    4.0  9.9598e-1  4.0171e-3    0.1    0.3
 2     6.00    2.00    4.50   3.0 .8750 Ex  1.9   3.2285e-3    3.0  9.9523e-1  2.9857e-3    0.0    1.1
 2     6.00    2.00    4.50   3.0 1.125 Ex  1.9   3.2249e-3    3.5  9.9411e-1  3.4794e-3    0.0    0.3
. . .
```

Data columns in the CR .AVG file are defined as follows:

skp	skip flag
Tx	Transmitter Dipole, station number of lowest numbered end.
Rx	Receiver Dipole, station number of lowest numbered end.
PltPt	Plot Point, station number at the midpoint between Tx and Rx.
NSp	N-Spacing, relationship between Tx and Rx, plotted as Y-Coordinate.
Freq	Frequency at which data was measured. If Freq=0, values are coupling corrected
Cmp	Component measured: Ex, Ey, Ez, Hx, Hy, Hz
Amps	Average SquareWave transmitter Current in amps, as entered into the GDP.
Resistivity	Average Fourier magnitude, divided by the SquareWave Current v/a.
Phase	Average Phase angle, in milliradians. If Freq=zero, values are coupling corrected.
Real	X-component of Rectangular coordinates, normalized to 1.0 at the Reference Freq.
Imag	Y-component of Rectangular coordinates, normalized by same value as for Real.
%Mag	Statistical variation of the data averaged for this data point.
sPhz	Statistical variation of the data averaged for this data point.

TDIP CFG Files: Time-domain IP survey configuration

TDIP CFG files hold one or more survey configuration descriptions. They are ASCII text files with an Oasis-montaj, parameter-group format. Survey configuration files have a hierarchical format with bracketed parameter group names, followed by lists of keyword, value pairs. New parameter groups or keywords may be added without disrupting existing programs. Programs ignore unrecognized parameter groups or keywords and attempt to supply reasonable default values for missing keywords.

To keep a clear distinction between coordinate systems; east, north and elevation are referred to as (x,y,z) coordinates; a moving coordinate system fixed to the geophysical equipment or cart is labeled (u,v,w); and individual loop shapes are described with an (a,b,c) coordinate system, which may be rotated relative to cart (u,v,w). Geosoft's Oasis montaj and most other plotting packages put the x plotting axis to the right and y positive upwards, so it is conventional to use

x=grid east, y=grid north and z=positive upward for geographic coordinates. (u,v,w) coordinates relative to the cart's reference point have: u in the direction of cart forward motion, v to the port side, and w upward. Cart (u,v,w) coordinates are fixed to the cart and are rotated and shifted with respect to geographic (x,y,z) as the cart moves. Loop wire corner coordinates are specified in (a,b,c) m, where (a,b,c) is a right-handed coordinate system which may be offset (loop center u, v, w) and rotated (loop yaw, pitch, roll) with respect to the cart's (u,v,w) reference point.

List of CFG File Parameters

```
[PARAMS_GLOBAL]                 = global parameter group
DIST_UNITS,m                    = length units (default=m,ft)
JOB_NAME,"DynamicNanoTEM"       = project name
JOB_FOR,"ESTCP"                 = customer name
JOB_BY,"Zonge Engineering"      = contractor name
JOB_NUMB,"RD21"                 = job number
JOB_DATE,"May/02"               = data acquisition date

 [MTDREDUCE]                    = MTDReduce parameter group
GPS_FILE,"DNTdemo.gps"          = gps dir\file name
GDP_TIME_OFFSET,0               = gdp synchronization time offset (sec)
GPS_TIME_OFFSET,13              = gps synchronization time offset (sec)
MAX_TIME_GAP=15                 = maximum time gap allowed during gps x,y,z interpolation
WRITE_BIN,1                     = 1 = write data to binary file, 0 = don't write
WRITE_CSV,0                     = 1 = write data to csv file, 0 = don't write
POLARITY_FLIP_1,0               = 1 = reverse polarity of Rx dipole 1 data while loading
POLARITY_FLIP_2,0               = 1 = reverse polarity of Rx dipole 2 data while loading

[HDW_CONFIG_01]                 = hardware config. parameter group
U_GPS,0.2                       = gps antenna offset from reference point (m)
V_GPS,0.0
W_GPS,0.0
REF_HEIGHT,0.266                = reference point height (m)
TX_REF_CHN=8                    = GDP channel used for current reference
TX_REF_RES=1                    = reference channel resistor (ohms)
TX_DIPOLE_ID=TX_DIPOLE_1        = Tx dipole parameter group name
NUMB_RX_DIPOLE,7                = # Rx loop
RX_DIPOLE_ID_1=RX_DIPOLE_101    = Rx dipole parameter group name
RX_DIPOLE_ID_2=RX_DIPOLE_102
RX_DIPOLE_ID_3=RX_DIPOLE_103
RX_DIPOLE_ID_4=RX_DIPOLE_104
RX_DIPOLE_ID_5=RX_DIPOLE_105
RX_DIPOLE_ID_6=RX_DIPOLE_106

[TX_DIPOLE_01                   = Tx dipole parameter group
NUMB_VERTEX,2                   = number of Tx wire segment endpoints
UV1,-0.5                        = negative current electrode u coordinate (m)
VV1,-0.5                        = negative current electrode v coordinate (m)
WV1=0                           = negative current electrode depth coordinate (m)
UV2,0.5                         = positive current electrode u coordinate (m)
VV2,0.5                         = positive current electrode v coordinate (m)
WV2=0                           = positive current electrode depth coordinate (m)

[RX_DIPOLE_101]                 = Rx dipole parameter group
U_CENTER=0                      = Rx dipole center u coordinate (m)
V_CENTER=-1.5                   = Rx dipole center v coordinate (m)
```

```
W_CENTER=0                      = Rx dipole center depth coordinate (m)
NUMB_VERTEX=2                   = number of dipole wire segments
UV1=0.25                        = negative electrode u coordinate (m)
VV1=-1.5                        = negative electrode v coordinate (m)
WV1=0                           = negative electrode depth coordinate (m)
UV2=-0.25                       = positive electrode u coordinate (m)
VV2=-1.5                        = positive electrode v coordinate (m)
WV2=0                           = positive electrode depth coordinate (m)

[RX_LOOP_01]                    = Rx loop parameter group
[WIN_CONFIG_1]
TX_DUTY=50
TX_FREQ=8
NCYCLE=1
NUMB_TIME_WINDOW=12
 [WIN_CONFIG_01]
TX_DUTY,50                      = Tx duty cycle (percent)
TX_FREQ,32.0                    = Tx repetition rate (hertz)
NUMB_TIME_WINDOW,12             = number of time windows
DELAY01=4.500                   = time wrt end of Tx ramp (msec)
. . . . .
DELAY12=30.63
WIDTH01=2.375                   = time window width (msec)
. . . . .
WIDTH12=2.375
```